1-1-2009

Investigating the effect of micro-CT radiation dose on tumour growth in mice

Kyle Foster
Ryerson University

INVESTIGATING THE EFFECT OF MICRO-CT RADIATION DOSE ON TUMOUR GROWTH IN MICE

By

Kyle Foster

B.Sc., University of Waterloo 2006

A thesis

presented to Ryerson University

In partial fulfillment of the

requirements of the degree of

Master of Science

in the program of

Biomedical Physics

Toronto, Ontario, Canada, 2009

Authors Declaration

I hereby declare that I am the sole author of this thesis. I authorize Ryerson University to lend this thesis to other institutions or individuals for the purpose of scholarly research.

Kyle Foster

I further authorize Ryerson University to reproduce this thesis by photocopying or by other means, in total or in part, at the request of other institutions or individuals for the purpose of scholarly research.

Kyle Foster

Investigating the Effect of Micro-CT Radiation Dose on Tumour Growth in Mice

Kyle Foster
M.Sc., Biomedical Physics, Ryerson University, 2009

Abstract

Micro-CT systems are used to obtain high-resolution CT images of small animals *in vivo*. The physical principals of x-ray CT require that the radiation dose delivered to the subject increase rapidly to achieve finer resolution while maintaining image quality.

The effect of micro-CT imaging dose on tumour growth in mice was investigated in a longitudinal imaging study. Four groups of tumour bearing mice were used: a control group that received no radiation and three unique imaging groups that received low, medium and high dose scans respectively. The mice underwent their imaging protocols four times, once every four days starting the fourth day post inoculation. The results of an ANOVA test indicate the serial imaging did not cause a statistically significant difference in tumour growth among the four groups. The notion that serial imaging causes an effect equivalent to radiotherapy treatment can confidently be rejected ($\alpha = 0.1$, $\beta = 0.1$).

Acknowledgements

Foremost, I would like to express my sincere gratitude to my supervisor Dr. Nancy Ford for her superb guidance and support throughout this project. I am truly grateful for the experience and knowledge she has passed to me during my time at Ryerson. I am a better scientist for it.

I would like to acknowledge the members of my supervisory committee, Dr. Ana Pejović-Milić and Dr. Pedro Goldman for many useful discussions and the support of my academic career.

I must acknowledge the enormous efforts of the entire staff at the Animal Resource Centre in the MaRS building. The staff and veterinarians cared for all the animals throughout the study. I would like to specifically acknowledge the director, Roberto Lopez, who performed the inoculations, assisted with the necropsies, and personally took interest in my work. This project could not have happened without the ARC staff.

I also owe many thanks to Dr. Min Rui for her expertise in the biology lab and Mr. Leo Zambito for keeping me running.

I would like to thank Richard Clarkson and Lisa Di Diodato for the many hours spent assisting and training me on the scanner.

Finally I would like to acknowledge the staff, faculty and students in the Physics Department at Ryerson, for giving me a home away from home to study in.

To my wife Laura,

for always keeping my heart and belly full.

Table of Contents

List of Tables

List of Figures

Nomenclature

I_0	Initial x-ray intensity (photons/mm^2)
I	Outgoing x-ray intensity (photons/mm^2)
μ	Linear attenuation coefficient (cm^{-1})
t	Thickness of an image subject (cm)
f(x,y)	Unknown distribution of attenuation coefficients
ℓ	X-ray detector coordinate
θ	X-ray detector angle, measured from the x-axis
$g(\ell,\theta)$	Projection values
$B_\theta(x,y)$	Backprojection image at detector angle θ
$\mu_B(x,y)$	Backprojection summation image
h	Hounsfield unit (HU or CT#)
m_e	Mass of electron (9.11×10^{-31} kg)
a_e	Acceleration of the electron (m/s^2)
e	Elementary charge (1.6×10^{-19}C)
Z	Atomic number (of anode material)
ε_0	Permittivity of free-space (8.85×10^{-12} C^2/N•m^2)
r	Distance between the electron and the anode nucleus (m)
σ_μ^2	Variance of linear attenuation coefficient in a uniform substance
σ_μ	Standard deviation of linear attenuation coefficient in a uniform substance
m	Number of projection views
N	Number of detected x-rays
ΔR	Sample spacing
C	Local contrast
μ_t	Linear attenuation coefficient of the object of interest

μ_b	Linear attenuation coefficient of the background
μ_m	Measured linear attenuation coefficient
P	Primary x-ray fluence of the transmitted beam
S	Scattered x-ray fluence of the transmitted beam
P_0	Primary x-ray fluence of the unattenuated beam
S_0	Scattered x-ray fluence of the unattenuated beam
M	Magnification factor
R	Smallest achievable pixel size
PBS	Phosphate buffered saline
EDTA	Ethylenediamine tetra-acetic acid (used to detach adherent cells in culture)
DMEM-10	Dulbecco's modified eagle's medium supplemented with 10% fetal bovine serum
HBSS	Hank's balanced salt solution
X	Exposure (R)
M_{raw}	Raw meter reading (nC)
M_c	Corrected meter reading (nC)
N_X	Calibration coefficient (R/nC)
P_{ion}	Correction factor for incomplete collection of ions
P_{pol}	Correction factor for changes in ion chamber polarity
P_{elec}	Electrometer specific correction factor
P_{rp}	Correction factor for radial variation in radiation field intensity
P_{TP}	Correction factor for air temperature and pressure
P_{leak}	Correction factor for leakage current
m_a	Mass of air within the chamber sensitive volume (kg)
f	Effect size
σ_m	Standard deviation of group means

σ	Pooled standard deviation
n_i	Size of group i
m_i	Mean tumour volume of group i
m	Overall mean tumour volume
N_T	Total sample size
D	Standardized range of means
m_{max}	Largest mean group tumour volume
m_{min}	Smallest mean group tumour volume

Chapter 1

1. Introduction

Since Wilhelm Roentgen (1845-1923) discovered x–rays in 1895 and published the famous image of his wife's hand, x-rays have played a key role in medical imaging. Radiography quickly became widespread and has remained an important medical imaging modality even today. Arguably the largest step forward in x-ray imaging was the invention of x-ray Computed Tomography (CT) in the early 1970's by Allan M. Cormack (1924-1998) and Sir Godfrey N. Hounsfield (1919-2004). These men pioneered work in computed tomography with contributions to the mathematical implementations for tomographic reconstruction and proof of principle prototypes, eventually earning them the 1979 Noble Prize for Medicine.

Developments in CT have obviously not stopped there; in fact CT scanners have evolved through several generations. First generation CT scanners used a pencil beam of x-rays and a single detector that had to be translated across the subject in order to obtain the data for a single view. Second generation scanners employed a fan beam with multiple detectors, while third and fourth generation scanners built on this theme but used a source and detector that rotates around the subject, drastically reducing the scan times. Further engineering developments lead to spiral CT, which takes advantage of a patient table that

can be translated through the scanner making it possible to quickly image a large region of the patient. Today's modern clinical CT scanners use a cone beam of x-rays, which allows for truly volumetric imaging and very fast scan times. Many modern systems also record a time signal, which allows for gated imaging, used to reduce organ motion artefacts in the acquired images.

Because of the massive popularity and utility of CT in clinical practice, it is easy to see why researchers doing work in a preclinical setting would be attracted to using this tool. Preclinical medical researchers who are interested in this type of imaging are typically involved in research with small lab animal subjects such as mice and rats.

Imaging small animals presents some new challenges not faced in the clinical setting. The largest obstacle is the fact that the anatomy of the lab animals is much smaller than that of a human subject, placing a very high demand on the resolution capabilities of the system. The fine resolution required for preclinical imaging forced engineers to develop smaller and smaller electronics for the detection of x-rays, leading to the flat panel detectors found in many systems today. Techniques for the production of x-rays have been refined as well with developments such as carbon nanotube electron sources (Liu *et al.* 2006) and micro-focus x-ray tubes with spot sizes as low as 5 μm (Wang and Vannier 2001).

Over the past several years engineers have been facing these problems and today we have access to micro-CT systems that can quickly produce images with voxel spacings of 0.15

mm and smaller, representing a better than 10 fold improvement in resolution over a typical clinical system.

However, these improvements do not come without some tradeoffs. While the engineering problems faced by micro-CT have been tackled with tremendous success, it is impossible to avoid the underlying physical principals of x-ray CT. These principals include using ionizing radiation (required for its transmission through the subject) to form the images, and in the case of micro-CT, focusing this radiation in order to acquire useful images at a fine resolution.

As with any medical imaging technique it is important to be aware of how the imaging modality is interacting with the subject and what affect the imaging itself may have on a patient. In the case of CT, where ionizing radiation is employed, it is important to be aware the subject will be imparted with a dose of radiation. In a clinical setting, the radiation dose to a human subject is quite low and the associated risk is far outweighed by the benefits of the medical information obtained. In the case of micro-CT, where the radiation dose to the subject is significantly higher, the question of the effect of imaging is being raised.

1.1. Principles of CT

1.1.1. X-ray Production

Apart from micro-CT systems set up at synchrotron light sources, all micro-CT systems employ an x-ray tube to generate x-rays. An X-ray tube consists of four major components: a cathode, an anode, an electron source (filament) and the vacuum it is situated in. Figure 1.1 depicts a simple schematic of a typical x-ray tube.

Figure 1.1 X-ray tube schematic featuring the major components: cathode, anode, filament and vacuum.

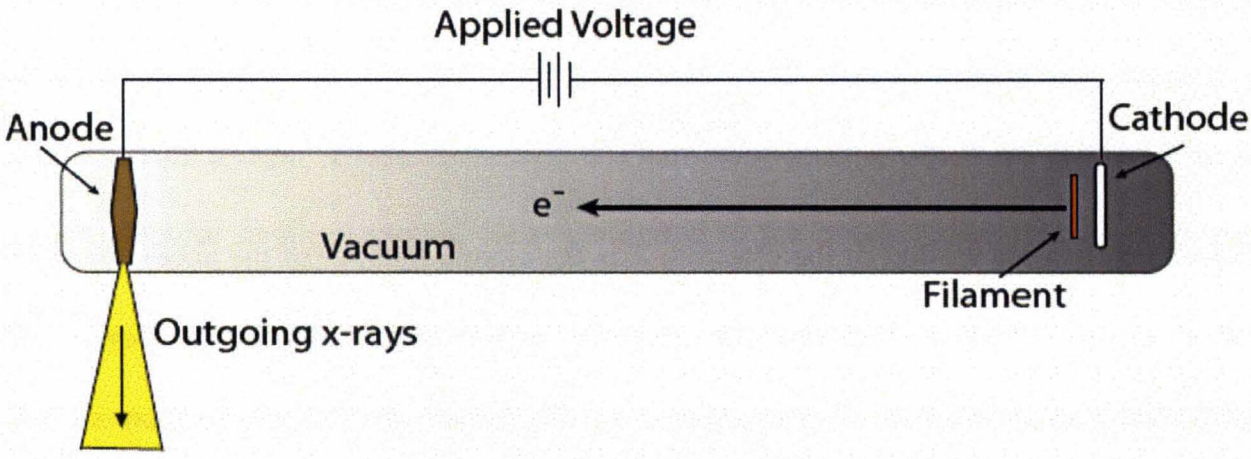

As the filament is heated, electrons are ejected via thermionic emission. These free electrons are then accelerated through the vacuum by the potential difference set up between the cathode and anode. When the electrons arrive at the anode they have kinetic energy in electron volts, numerically equal to the tube voltage in volts. This kinetic energy is converted to heat and x-rays in the anode as the electrons undergo Coulomb

force interactions with the nuclei of the anode material. Any x-rays produced this way are referred to as Bremsstrahlung x-rays.

As an electron passes by the positively charged nucleus of an atom of the anode material, it will experience a Coulomb force attraction causing the electron to deflect toward the nucleus. The acceleration experienced by the electron can be determined classically by equating Newton's force law to the Coulomb force:

$$m_e a_e = \frac{e(Ze)}{4\pi\varepsilon_0 r^2}, \tag{1.1}$$

revealing,

$$a_e \propto \frac{Z}{r^2} \tag{1.2}$$

where a_e is the acceleration of the electron, Z is the atomic number of the anode material and r is the distance between the electron and nucleus. Since the *power* of Bremsstrahlung production is proportional to the square of the acceleration of the electron (the Larmor relationship), we would like to maximize the electron's acceleration.

Equation 1.2 shows the acceleration of the electron is proportional to the atomic number of the anode material, Z, and inversely proportional to the square of the distance between them, r. As the electrons strike the anode, we have no control over the distance between the electrons and the nuclei; however by selecting a high Z material for the anode, we can optimize the efficiency of x-ray creation.

Producing Bremsstrahlung x-rays is rather inefficient. X-ray tubes used to generate x-rays in the diagnostic range (40-120 keV) will only convert about 1% of the electron kinetic energy into x-rays, while the remaining energy is lost as heat (Podgorsak 2006). All the heat produced by running an x-ray tube can easily damage the anode or x-ray tube if the operator is not careful. The heat generated also places another requirement on the anode material – it must have a high heat capacity. With high atomic number (Z) and high heat capacity in mind, the anode material of choice for most x-ray tubes is Tungsten.

The photons in a Bremsstrahlung beam from an x-ray tube running at a voltage of V volts will have a continuous range of energies starting from a maximum of V electron volts and falling lower, out of the energy range of x-rays on the electromagnetic spectrum. As depicted in Figure 1.2, the Bremsstrahlung beam will also include a large number of characteristic x-rays. These are x-rays of a particular energy, which are produced by the anode material itself as excited electrons bound to the anode atoms transition between shells.

For the purposes of CT imaging only the x-rays that have a chance of being transmitted through the subject are useful. The low energy photons produced in the x-ray tube, which have no chance of penetrating the entire subject, are therefore filtered out of the beam. Some beam filtering occurs in the components of the x-ray tube itself; however additional filtering is usually required. The additional filtering is typically achieved by placing a metal foil (such as copper), less than 1 mm thick, in the path of the beam. Filtering out the low energy x-rays also serves to improve the dose efficiency of a CT

system by removing photons that would otherwise contribute x-ray dose to the subject while having little or no chance of contributing to the image signal.

Figure 1.2 A typical Bremsstrahlung beam spectrum, featuring the characteristic x-ray lines of tungsten found at approximately 60 and 70 keV.

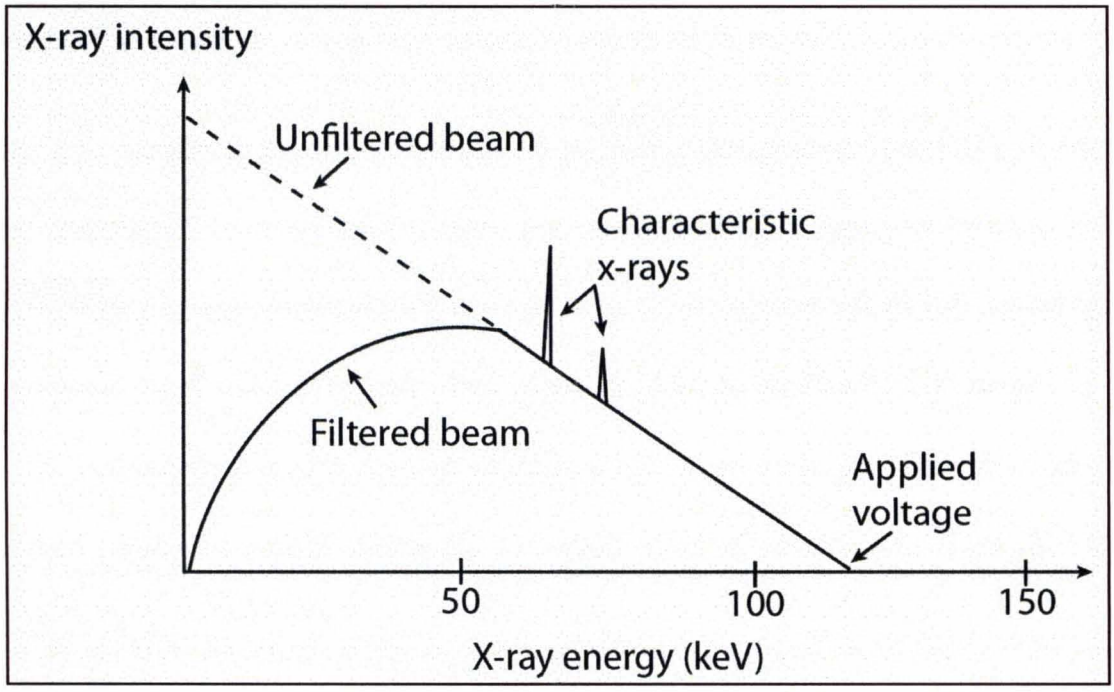

1.1.2. X-ray Interactions with Matter

There are over a dozen different processes by which a photon can interact with matter (Podgorsak 2006). The likelihood of any one of the processes occurring depends a great deal on the energy of the photon and the atomic make up of the material. In terms of the photon energies and materials of concern to clinical or preclinical CT physics, the most important photon interactions are the photoelectric effect and Compton scattering.

Photoelectric Effect

When a photon interacts with an atom via the photoelectric effect, the photon is completely absorbed by an inner shell electron, causing this electron to be ejected from the atom (Figure 1.3). In this case, the now free electron (referred to as a photoelectron) has an initial kinetic energy equal to the energy of the incoming photon less the binding energy of the shell it was in.

Figure 1.3 Pictorial representation of the photoelectric effect. An inner shell electron absorbs the incoming photon. The inner shell electron is ejected and replaced by an outer shell electron. The outer shell electron emits a characteristic photon as it transitions between shells.

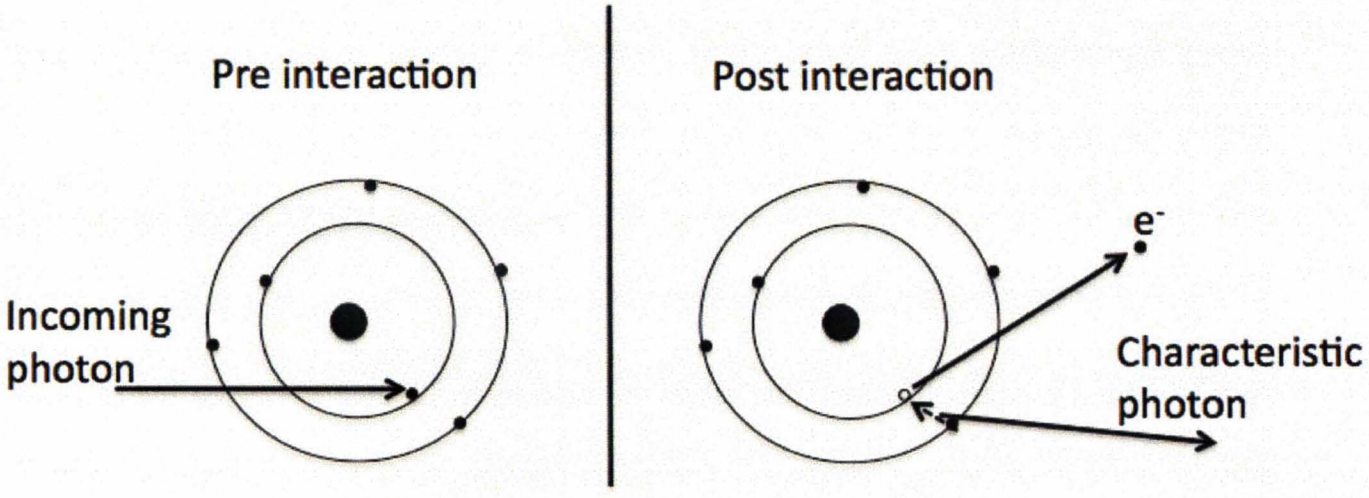

The vacancy left at the inner shell is quickly filled by an electron in the outer shell of the atom. As this electron drops toward the nucleus, it emits a characteristic photon with energy equal to the magnitude of the difference in binding energies of the two shells.

X-rays undergoing the photoelectric effect do not reach the x-ray detector of a CT system, and therefore they do not contribute to the signal recorded by the detector. Instead these x-rays deposit their energy in the subject, contributing to the absorbed radiation dose.

Compton Effect

The Compton effect is characterized by the interaction of a high-energy photon with a loosely bound orbital electron (Figure 1.4). In this case the photon is *not* absorbed, but instead it is scattered at a different angle and wavelength after imparting some of its energy to the electron. The energy imparted to the electron is much greater than the electron's binding energy causing the electron to be scattered away with initial kinetic energy approximately equal to the energy given by the photon. In this case, the scattered photon can go on to interact with other atoms in the material or perhaps reach the detector. The recoil electron will quickly deposit its kinetic energy in the subject via Coulomb interactions, contributing to the subject dose.

Any Compton scattered photons that reach the detector will serve to reduce the contrast *and* the noise in the images produced. The effect of Compton scatter on image quality is discussed in more detail in section 1.1.5.

Figure 1.4 Pictorial representation of the Compton effect. The incoming photon imparts energy to the outer shell electron. The electron is ejected and the photon is scattered in a different direction at lower energy.

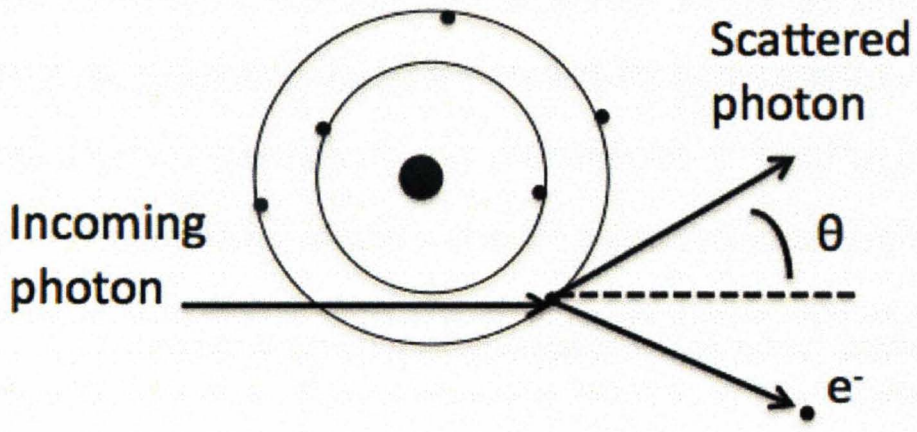

1.1.3. Flat Panel x-ray Detection

X-ray detection has evolved a great deal from the grainy film originally used by Roentgen in the late 1800's. Modern CT systems employ an area array of solid-state x-ray detectors to acquire a digital signal. These detectors have been termed flat panel detectors.

Flat panel detectors are based on semi-conductor technology. One such design employs a scintillation screen placed directly in front of the semi-conductor electronics. As the x-rays pass through the scintillation screen, they are converted to many lower energy photons. These newly created photons then propagate toward the semi-conductor where

they interact with the electrons of the material. The simple semi-conductor model as described by Knoll (2000) and depicted in Figure 1.5 provides a conceptual description the behavior of these electrons as they interact with the photons.

In this model, semi-conductors are assumed to have three important energy ranges: the valence band, the band gap and the conduction band. Electrons in the valence band are loosely bound to atoms of the semi-conductor. No electrons have energy that lies in the range of the band gap, while the electrons with energy in the range of the conduction band are essentially free electrons, which are mobile within the semi-conductor.

Figure 1.5 The band gap energy model of semi-conductor x-ray detection.

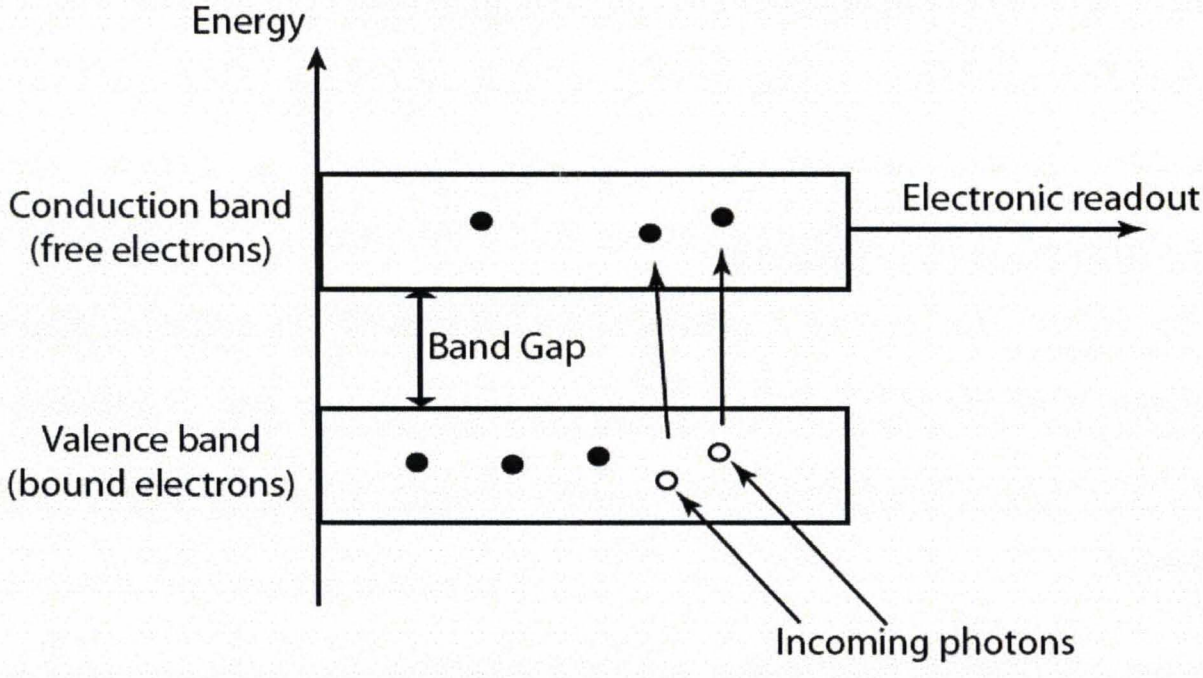

When a photon interacts with an electron in the valence band of the semi conductor, the electron will gain the energy provided by the photon. If the energy gained is enough to

overcome the band gap, this electron will be promoted to the conduction band of the semi-conductor. Applying a small voltage across the semi-conductor easily collects the electrons residing in the conduction band. The total charge collected is proportional to the number of x-rays impinging on a given element of the detector, and thus the intensity of the x-rays can be measured.

Advances in semi-conductor fabrication and the miniaturization of electronics has allowed for the production of x-ray detector arrays featuring individual detection elements in the range of 100-200 μm^2. Detectors based on this design also have the advantage of short readout times. For example, the system used for preclinical imaging described by Ross *et al.* (2006) can readout 160 rows of 1024 detectors in 4 ms. These short readout times make these detectors a good choice for gated image acquisition.

1.1.4. Image Reconstruction

X-ray CT images are generated based on the relative transmission of x-rays through the subject. Different structures such as bone, muscle and fat attenuate x-rays by different amounts and a CT image is ultimately a map of these attenuations. CT image reconstruction techniques are a research field of their own. The most important image reconstruction technique from a conceptual standpoint is the backprojection algorithm described below.

As x-rays pass through a subject they are attenuated by different amounts, depending on what materials or structures were along the path. The *amount* of attenuation exhibited by a given material is called the linear attenuation coefficient, μ, typically measured in units

of cm^{-1}. In the ideal case of a 1D homogenous material with thickness t and linear attenuation coefficient μ, the attenuation of monochromatic x-rays is described by Lambert-Beers law:

$$I = I_0 e^{-\mu t}, \tag{1.3}$$

where, I is the transmitted intensity and I_o is the incident intensity. In the case of a heterogeneous material, the attenuation is described by generalizing the Lambert-Beers law to accommodate varying liner attenuation coefficients. In this case:

$$I = I_0 e^{-\int \mu(t)dt}. \tag{1.4}$$

Rearranging Eq. 1.4 reveals:

$$\int \mu(t)dt = \ln\left(\frac{I_0}{I}\right), \tag{1.5}$$

CT imaging takes advantage of the relation in equation 1.5 by taking measurements of I and I_o, revealing the integrated value of the linear attenuation coefficients along the path of the x-rays. This value is referred to as a projection.

In order to understand how images are formed, the idea of x-ray projections must be extended to two dimensions as depicted in Figure 1.6. In this case we have an unknown two dimensional distribution of attenuation coefficients f(x,y) (which we are trying to find) and the x-ray detector along the ℓ-axis at an angle θ to the x-axis.

Figure 1.6 Diagram of the coordinate systems used to describe the Radon transform and backprojection reconstruction.

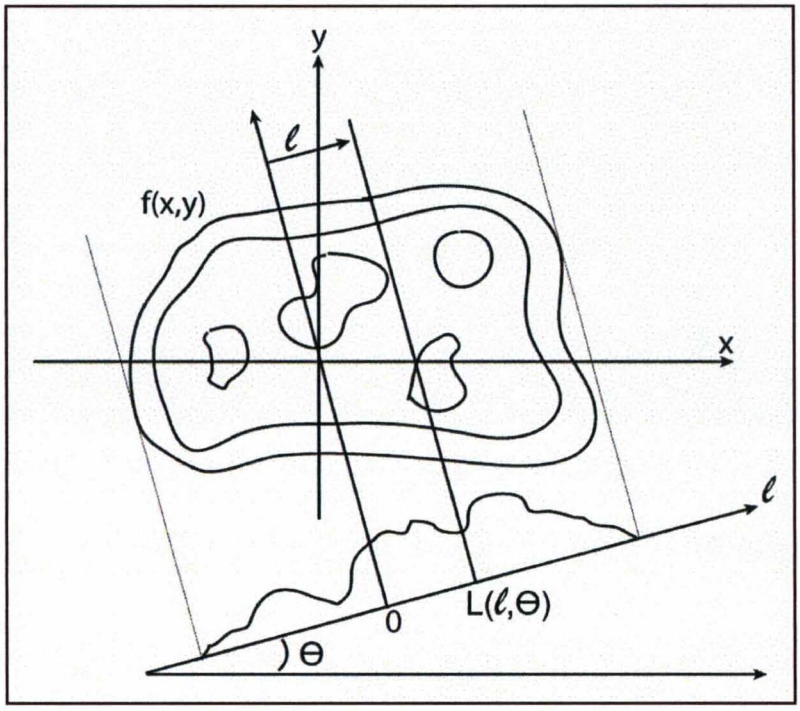

This description of image reconstruction assumes the x-rays are all travelling parallel to one another. The projections along lines perpendicular to the detector at position ℓ and angle θ are equal to the line integral of f(x,y) along the straight line $L(\ell,\theta)$. This is described mathematically by the 2D Radon transform:

$$\ln\left(\frac{I_0}{I}\right) = g(\ell,\theta) = \int_{-\infty}^{\infty}\int_{-\infty}^{\infty} f(x,y)\delta(x\cos\theta + y\sin\theta - \ell)dxdy \qquad (1.6)$$

The delta function has the effect of causing the integrand to be zero everywhere except on the line $L(\ell,\theta)$. The function $g(\ell,\theta)$ contains the *projection values* along the lines $L(\ell,\theta)$.

Once the Radon transform data has been gathered by the scanner over a range of angles (at least π radians in this formulation) and all pertinent ℓ values, the CT image can be formed by *backprojecting* the projection values along the lines they were acquired over. Backprojecting essentially assigns the total integrated projection value to every point along the line it was gathered over (Figure 1.7 – B). For a given detector angle of θ, the *backprojection image* is given mathematically by:

$$B_\theta(x,y) = g(x\cos\theta + y\sin\theta,\theta) \tag{1.7}$$

When these backprojection images are summed up over all angles θ, the *backprojection summation image* is formed (Figure 1.7 - C). This image as defined by:

$$\mu_B(x,y) = \int_0^\pi B_\theta(x,y)d\theta \tag{1.8}$$

where μ_B(x,y) is the reconstruction of the original unknown distribution f(x,y). The reconstructed image is not an exact replication of the unknown distribution because the backprojection technique as described induces some blurring in the acquired image. This entire process will result in an image representing a single 2D slice throught the subject.

Figure 1.7 Example images of backprojection reconstruction. A) The original distribution of points, f(x,y). B) A single backprojection image, $B_\theta(x,y)$. C) The final backprojection summation image, $\mu_B(x,y)$. Images adapted from Prince 2006.

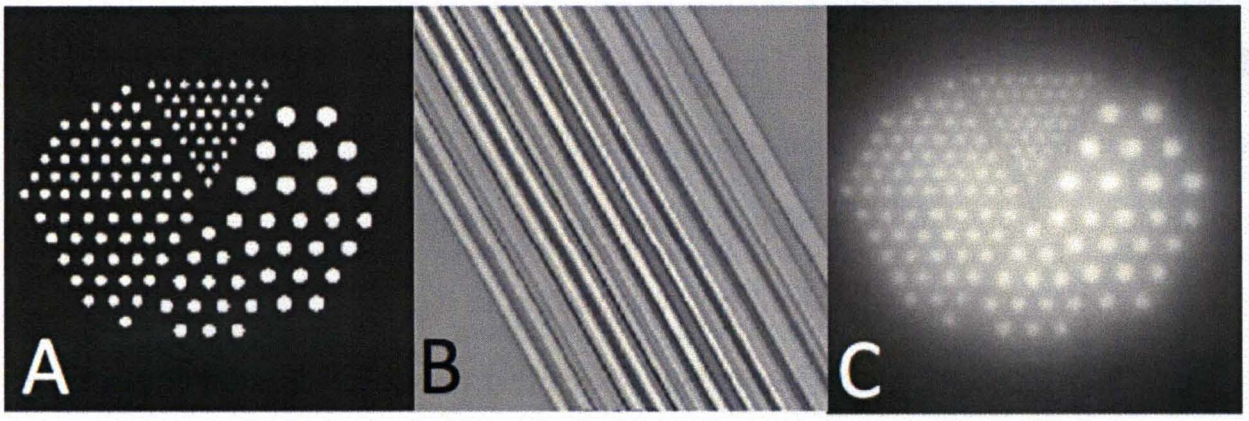

In order to obtain a 3D data set from a CT scanner, successive 2D image slices through the subject are 'stacked' to form a 3D image. Whereas a regular 2D digital image is comprised of pixels (the smallest element of the image, a square or rectangular area containing a uniform colour or greyscale value), a 3D image is comprised of so-called *voxels.* A voxel is the smallest element of a 3D image, a rectangular prism or cubic volume containing a uniform value.

This description of image formation provides a solid conceptual understanding of the standard backprojection algorithm. Many advances have been made in the field of CT image reconstruction, extending this concept from parallel x-ray beams, to fan and cone beams (Feldkamp *et al.* 1984).

All but the most basic reconstruction algorithms also include many signal processing steps such as filtering the data to reduce the inherent blurring and statistical noise. One

such reconstruction algorithm is called filtered backprojection. This algorithm is very similar to standard backprojection, however a data filtration step is added. After the projection data has been acquired, the data is convolved with a filter function to optimize the image. Many different filter functions exist (such as the ramp filter, Hanning filter and Weiner filter) each with their own characteristics. The choice of filter function will determine the degree of 'smoothing' (reduction in noise) in the reconstructed image. Highly smoothing filters will blend any sharp edges in the image, greatly reducing the noise at the expense of image resolution. Filters that provide minimal smoothing can maintain image resolution however they do not provide the same reduction in image noise. In practice, all CT image reconstruction will include some data filtration.

Reconstructed CT images are simply maps of the attenuation throughout the subject. Since different CT systems operate at different energies using different detectors and hardware, each system will provide a numerically different value of μ for the same structure in a given subject. For this reason, it is desirable to have a standard scale in order to compare data from different systems. This scale is referred to as the Hounsfield Scale and the Hounsfield Unit (HU) for a given attenuation μ (also referred to as the CT#) is defined by:

$$h(\mu) = 1000 \cdot \frac{\mu - \mu_{water}}{\mu_{water}}. \tag{1.9}$$

From this definition it is clear that water has $h = 0$ HU while air (which has negligible linear attenuation, $\mu \approx 0$) has $h = -1000$ HU. In terms of biological structures, bone is the most attenuating and has CT# $\approx$ 2000 HU.

1.1.5. Noise, Contrast and Signal Strength in CT

Noise in x-ray CT can be understood as the fluctuation of CT numbers (or linear attenuation coefficient) between voxels in an image of a uniform substance. Faulkner and Moores (1984) developed a model to calculate the variance in linear attenuation coefficient at the centre of a uniform cylinder. This idealized model does not include sources of noise inherent to the CT system, such as noise from the electronics or detectors. They were able to show that the variance is given by:

$$\sigma_{\mu}^{2} = \frac{\pi^{2}}{12mN\Delta R^{2}} \tag{1.10}$$

where m is the number of projection views, N is the average number of detected x-rays per view and ΔR is the sample spacing (ΔR is equal to the detector spacing at the minimum).

There are two important trends to notice in this relation; firstly, the variance, is inversely proportional to the number of x-rays recorded by the detector. This implies that increasing the number of photons passing through the subject can reduce the noise in the image. However, this in turn means increasing the dose to the subject. In the case of *ex vivo* imaging or specimen imaging, one can take advantage of this relation to acquire low

noise images by increasing x-ray fluence or scan time. In the case of *in vivo* imaging this is a tradeoff that must be handled with care. The dose delivered to the subject should be kept to a minimum; however, the scan must also provide a *useful* image.

The second trend to consider is that the variance is inversely proportional to the square of the sample spacing. This relation highlights one of the major problems faced by high resolution CT imaging. For a fixed dose to the subject, the noise in the image will quickly rise as the x-ray detector elements become smaller (as required to obtain finer resolutions). The only way to combat this effect is to increase the number of photons reaching the detector, thereby increasing the dose to the subject.

The contrast in an image is what allows one to differentiate between structures. Contrast in CT images ultimately arises from differences in the linear attenuation coefficients among the structures within the subject. The local contrast in a CT image is defined as the difference in linear attenuation coefficients between the target and background structures relative to the attenuation coefficient of the background structure. Mathematically, the contrast is defined as:

$$C = \frac{\mu_t - \mu_b}{\mu_b}, \tag{1.11}$$

where μ_t is the target attenuation and μ_b is the background attenuation. Adequate image contrast is essential in oncology related applications of radiology where it is often the goal to distinguish between tissues with similar linear attenuation.

The contrast and noise present in an image are two of the most important quantities to consider when describing the quality of an image. The differential signal-to-noise ratio (SNR_{diff}) combines the contrast and noise into a single quantity that can be used to assess image quality. The differential SNR is defined by

$$SNR_{diff} = \frac{C\mu_b}{\sigma_\mu}. \tag{1.12}$$

The differential signal to noise ratio is interpreted as the difference in target and background attenuation coefficients relative to the standard deviation of the measurement, σ_μ. It is the differential SNR that quantifies ones ability to differentiate an object from its surroundings in an image.

Improvements to the differential SNR can be achieved by reducing the number of scattered photons reaching the detector. This can be achieved by placing an attenuating grid above the x-ray detector. The grid acts to absorb any photons that are not impinging squarely on the face of the detector, such as those having undergone a Compton scattering event. Grids can effectively improve image contrast, however they come at the expense of increased exposure. Use of a grid will typically require an exposure 3-8 times larger (Prince 2006) to maintain image quality.

Johns and Yaffe (1982) showed that any scattered photons that do reach the detector cause the measured attenuation coefficient to underestimate the actual value. Consider the primary and scattered x-ray fluence (represented by P and S respectively) after the beam

has passed through a uniform object with attenuation μ and thickness t. The detector will measure an attenuation coefficient μ_m as described by:

$$\mu_m t = \ln\left(\frac{P_0}{P}\right) + \ln\left(\frac{1+S_0/P_0}{1+S/P}\right), \tag{1.13}$$

where P_0 and S_0 and the primary and scattered fluences of the unattenuated beam. Dividing both sides of Eq 1.13 by t, and taking advantage of Eq. 1.5, the measured attenuation coefficient is revealed as

$$\mu_m = \mu + \frac{1}{t}\ln\left(\frac{1+S_0/P_0}{1+S/P}\right). \tag{1.14}$$

The second term in Eq. 1.14 will always be negative because the ratio of scattered-to-primary photons in the unattenuated beam will always be lower than in the attenuated beam. As a result the measured attenuation μ_m will always be lower than the actual value μ.

Siewerdsen and Jaffray (2001) extended this approach, using it to show that scattered photons will always cause a reduction in the contrast available in the image. They also noted that scattered photons actually cause a reduction in image noise. This can be understood by referring to equation 1.10. Since the noise depends inversely on the number of photons detected, even scattered photons serve to reduce image noise.

1.2. Micro-CT

1.2.1. Achieving High Resolution in X-ray CT

Ultimately design factors such as scanner geometry, x-ray sources and x-ray detectors will define the capabilities of a particular CT system. However the laws of physics govern the relationships between factors such as image noise, spatial resolution, temporal resolution and contrast. These relations include inherent tradeoffs that make optimizing all image characteristics in a single system impossible. Therefore, in order to achieve the high resolutions desired in micro-CT, these systems make tradeoffs that offer better resolution at the expense of other parameters.

Bartling *et al.* (2007) pointed to one such tradeoff made when selecting the scanner geometry. If the source to object distance (SOD) is smaller than the object to detector distance (ODD), than the system will offer a magnification factor given by:

$$M = \frac{ODD}{SOD}, \tag{1.15}$$

This magnification is desired in micro-CT as it serves to improve the spatial resolution of the system. However the tradeoff is that as the SOD decreases, the x-ray spot size will cause increasing image blur, which in turn reduces the available resolution. Reducing the x-ray spot size can help to mitigate this negative effect, but reducing the x-ray spot-size comes with tradeoffs as well.

A small spot size is desirable for optimal resolution, but as the spot size decreases so does the rate of heat dissipation (Paulus *et al.* 2001). Because of the physical limit on heat

dissipation in the anode, a limit on the power delivered to the anode must also be in place. The power being delivered to the anode is given by the product of the tube voltage and current. Since these parameters also govern the x-ray flux being generated, the x-ray spot size and heat dissipation will ultimately limit the x-ray flux.

The tradeoff between x-ray spot size and x-ray flux poses a significant problem in small animal imaging. High x-ray flux is desired to reduce scan time and to limit the effect that the rapid organ motion associated with the breathing and heart beat of small lab animals has on the reconstructed images. However, this comes at the expense of increasing the x-ray spot size and therefore decreasing resolution. One approach to dealing with this tradeoff is to increase the scan time, thereby reducing the x-ray flux required. Again a tradeoff is being made, in this case at the expense of the user's time and resource.

Perhaps the most important balance to consider in micro-CT imaging is the relation between image noise and subject dose. Further consideration of the Faulkner and Moores model shows that the noise in the reconstructed images is inversely proportional to the x-ray fluence, ϕ, and the fourth power of the voxel spacing, as shown in Eq. 1.16.

$$\sigma_{\mu}^{2} \propto \frac{1}{\phi \Delta R^{4}} \tag{1.16}$$

Since the reduction in image noise in high resolution images comes at the expense of a large increase in dose, *in vivo* micro-CT images are usually acquired with noise levels of $\sigma_{\mu} \approx 40$ HU, which would be unacceptable in clinical use where the noise typically must not exceed $\sigma_{\mu} \approx 10$ HU.

The x-ray detection technology used plays a very important role in achieving high-resolution CT images. The pitch of the detector and the x-ray spot size are the two factors with the largest influence on the spatial resolution of the image (Bartling *et al.* 2007). For an otherwise ideal system, the smallest achievable pixel size, R, at the isocentre of the scanner would be given by:

$$R = \frac{\text{pitch}}{M}. \tag{1.17}$$

Because each detector element still requires a fixed number of photons to record a useful signal, the pitch of the detector determines the x-ray fluence required.

There are obviously many considerations that go into the design of a micro-CT system, depending a great deal on the application of the system. Where the researcher is not concerned with the dose delivered to the subject (such as in *ex vivo* specimen imaging), the tradeoffs required to achieve high quality images are easy to make. However the imaging of living subjects makes choosing the tradeoffs a more difficult task. Nonetheless, the preclinical use of micro-CT scanners to image lab animals has become a popular research tool, finding application in a broad range of study.

1.2.2. Current Preclinical Applications of Micro-CT

An important advantage offered by preclinical imaging such as micro-CT is the ability to track a single cohort of animals throughout an entire investigation, termed a *longitudinal study*, without the need to euthanize the animals at each measurement time-point. Following the same cohort of animals helps to reduce the impact of the variations

between animals and reduces the number of animals required to perform a study, thus offering the researcher an ethical and economical alternative.

Researchers focusing on preclinical investigations of bone disorders quickly adopted micro-CT. The fine resolution offered has allowed for quantitative investigation of bone disorders and bone healing both *in vivo* and *ex vivo*.

For example, Nyman *et al.* (2009) used micro-CT to analyze callus formation due to the healing of a femur fracture in rats. They were able to find correlations between quantitative measures of the callus volume and mineral density with other biomechanical properties of the callus such as the strength and stiffness. This information was used to confirm the efficacy of a bone healing intervention called Lovastatin. The imaging in this study was done on *ex vivo* samples of bone, and so the radiation dose to the sample is of little concern.

Because of the relatively slow changes seen in bone, micro-CT lends itself to longitudinal *in vivo* preclinical study of bone disorders. Work by Chun *et al.* (2006) investigated thickness of trabecular bone in ovariectomized rats over a ten-week period. The animals each received five scans over the ten weeks. Chun *et al.* were able to track the thickness of trabecular bone among three different groups of rats, showing a marked decrease in the bone thickness of the rats suffering from osteoporosis. Despite the fact that the imaging was performed *in vivo*, this group did not report the dose delivered to their subjects over the course of the study, although they do point toward reducing the scan time and subject dose in future work.

There has also been much interest in the use of micro-CT to produce so-called *gated images* of the cardiac or respiratory cycles of lab animals. Internal organ motion in small animals presents a challenge because of the very fast heartbeat and breathing rates (up to 632±51 and 163 repetitions per minute respectively in mice – www.med.yale.edu/yarc/VCS/normative.htm). In order to overcome this rapid motion and acquire clear images of the heart or lungs, researchers have employed prospective and retrospective image gating techniques.

Retrospective gating techniques such as those proposed by Sonke *et al.* (2005), Drangova *et al.* (2007) and Ford *et al.* (2007) are essentially data processing tools, which are used to reduce organ motion artefacts in the final image. The image views acquired by the scanner are recorded along with the *time* of their acquisition. During the scan, the subject's heart rate and breathing rate are also tracked and recorded against time. By doing this, the subject's physiological cycles can be compared to the acquisition time of the many views from the scanner. The final image can then be reconstructed based only on the data that was acquired during a given phase of the cycle of interest.

In order to acquire enough data for a single retrospectively gated image, the user typically has to acquire several full data sets, then sift through the data and reconstruct the specific phase. This approach has the drawback of delivering the radiation dose of several scans in order to acquire a single gated image.

Prospective gating is achieved by taking a real time reading of the subject's heart and breathing rate and feeding that data to the CT system in order to turn the x-rays on and

off. For instance the x-rays may only be on when the animal is at the full inspiration phase of breathing, thereby imaging the lungs when they are in a specific position only. Because the x-rays are only on during the required phase of the cycle, prospective gating techniques have the advantage of reducing the total dose to the subject while still acquiring gated images. This type of technique has been used in ventilated (Cavanaugh *et al.* 2004) and free breathing (Ford *et al.* 2005) animals to produce sharp images of the lungs used to assess lung tumour volume and detectability as well as lung morphology. Bedea *et al.* demonstrated the use of a prospectively gated imaging protocol to image the thorax of a mouse. They were able to show that the anatomic resolution in the gated images acquired *in vivo* was quite near to the resolution seen in when the same animal was imaged after being euthanized. This highlights the utility and importance of gated imaging protocols in small animal imaging.

Oncology models have also drawn interest for preclinical imaging. The opportunity to perform longitudinal studies of a single cohort of tumour bearing animals offers the researcher an economical and ethical advantage in study design. Tumour tissue usually offers little contrast with its surroundings (Weichert *et al.* 2000) leading many preclinical oncology studies to involve the use contrast agents when imaging, in order to clearly define tumour boundaries. The molecules of the contrast agents typically include iodine atoms. Iodine atoms are used because they are tolerated well by the subject and their high electron density provides excellent x-ray attenuation (Bakan *et al.* 1996).

Use of the hepatocyte-selective contrast agent ITG was demonstrated by Weber *et al.* (2004). This iodine-based contrast agent binds to the healthy liver cells, causing them to appear highly attenuating in the CT images, while leaving the tumour cells unchanged. Weber *et al.* showed accurate tumor size measurements using micro-CT with the appropriate contrast enhancement, while reporting the only false reading in images with poor contrast enhancement. Despite taking serial images of the tumour bearing animals, this study makes no mention of the radiation dose delivered by the scans.

Cavanaugh *et al.* (2004) demonstrated the use of respiratory-gated micro-CT for the measurement of lung tumours in mice. They were able to show a strong correlation between the number of tumours detected using micro-CT and necropsy as well as reproducible and accurate tumour volume measurements, leading them to conclude that *in vivo* micro-CT is a valuable tool for preclinical imaging.

The study by Cavanaugh *et al.* also revealed heterogeneity among the tumours of different mice, despite a uniform initiating event. Serial imaging also showed that some tumours grew while others shrank over the course of the investigation. This is an example of the information that can be gained through longitudinal imaging of the subjects. Cavanaugh *et al.* reported the dose to air at isocentre for the imaging protocol used as 14 cGy. This is a dose level similar to other published prospective respiratory-gated imaging protocols (Ford *et al.* 2005).

1.2.3. Radiation Dose Concerns Raised in Micro-CT Imaging

The fundamental unit of image information in x-ray CT is the number of photons that are recorded by the detector per unit resolution. Motz and Danos (1978) showed that a typical system needs 10^4 -10^5 photons to pass through a given region of interest (ROI) *per* unit resolution at the image plane in order to achieve a signal strong enough to overcome the statistical noise of the photons. Therefore, as the desired resolution over a given ROI becomes smaller, the x-ray flux must become greater; consequently the dose to the subject increases as well.

Ford *et al.* (2003) showed that in order to maintain image quality while achieving a tenfold reduction in voxel size, a 10^4-fold increase in radiation dose is required. Ultimately, this trend places a limit on the resolution of *in vivo* x-ray CT imaging. This obvious problem has stirred substantial interest by researchers who have used many different techniques to measure and estimate the dose delivered to the subjects of micro-CT scans.

Extensive computer modeling of the dose delivered to an animal subject by a micro-CT scan has been reported by Boone *et al.* (2004) and Taschereau *et al.* (2006). Boone provided parameters, based on a cylindrical phantom model, which can be used to estimate doses to specific organs. Taschereau performed a simulation with a more realistic mouse model and reported average whole body doses ranging from 8 cGy to 16 cGy for an anatomical micro-CT scan of a mouse, depending on protocol parameters.

Direct measurements of the delivered radiation doses have also been performed. Obenaus and Smith (2004) surgically implanted thermoluminescent detectors (TLDs) into euthanized mice and rats. TLDs were placed at the locations of several critical organs such as the brain, lung, heart, stomach, bladder and skin. All the animals received the same single micro-CT scan, a typical anatomical scan with an entrance dose of 6.5 cGy. The results indicated statistically significant decrease in radiation dose delivered to the internal organs compared with the dose to the skin, while the brain received the lowest dose because of the radioprotection offered by the skull. The average dose to tissue of a mouse from this scan was approximate 3.5 cGy.

While the dose from an anatomical scan is typically low (below 10 cGy), the dose delivered by a gated protocol will be greater. Respiratory-gated imaging protocols used on mice typically report delivering doses in the range of 15 cGy (Walters *et al.* 2004) to 19 cGy (Ford *et al.* 2005) depending on scan parameters. Cardiac gated imaging protocols used for mice require even greater doses to overcome the rapid heart rate. Cardiac gated protocols reported in the literature deliver entrance radiation doses as low as 28 cGy (Drangova *et al.* 2007) to acquire a set of images representing 7 phases of cardiac motion. One protocol reported delivering an entrance doses of 150 cGy (Badea *et al.* 2006) to acquire a data set consisting of 12 phases of cardiac motion.

Radiation doses this high certainly raise concern for *in vivo* imaging. 150 cGy of whole body irradiation represents a significant fraction of the LD50/30 for mice. The LD50/30 is the radiation dose, which is lethal to 50% of mice in 30 days, and it is in the range of

500 – 730 cGy (Ford *et al.* 2003). 150 cGy would also comprise a significant portion of the radiation dose delivered to a tumour as part of a radiotherapy treatment. As an example, Medina *et al.* (2008) used 250 cGy delivered to a subcutaneous tumour in mice as part of a preclinical radiotherapy treatment.

Since the radiation doses delivered by micro-CT scanners are approaching those used for in a single fraction of a radiation therapy treatment, it follows that a longitudinal imaging study, which repeatedly delivers these high radiation doses, could cause an effect on tumour growth in mice.

1.2.4. Experimental Motivation and Hypothesis

The radiation doses delivered during a micro-CT scan have caused many different groups to suggest using caution when performing longitudinal micro-CT imaging studies, (Obenaus and Smith 2004, Carlson *et al.* 2007, Figueroa *et al.* 2008) especially when the subject could display some sensitivity to the radiation (e.g. tumour bearing lab animals). It was this concern that provided the motivation for the work presented here.

The hypothesis tested was that the radiation dose delivered by a longitudinal micro-CT imaging study would cause an effect on the growth of tumours in mice. The description of the experimental methods, materials and results are presented in the following chapters.

Chapter 2

2. Methods and Materials

2.1. Mouse Model

A murine model of melanoma was used as the basis of this investigation. The mice used were 8-10 week old female C57BL/6 mice supplied by The Jackson Laboratory (Bar Harbor, ME). All the mice were housed four to a cage and kept in the Animal Resource Centre (ARC) within the Toronto Medical Discovery Tower (TMDT). The mice were kept in a holding room with automatic lighting on a two-phase cycle: 12 hours on – 12 hours off. The animals had full access to food and water and regular care provided by the ARC staff. Once the mice had acclimated to their new environment (at least 48 hours after arriving at the TMDT facility), each mouse was marked with an ear-tag and weighed on an electronic balance.

The tumour cell line used, B16F1, was selected for its high radiosensitivity (Bristow *et al.* 1990) and common use within the literature (Graham *et al.* 2005, Safwat *et al.* 2004 and Garcia-Barros *et al.* 2003). This cell line was originally derived from C57BL/6 mice, which alleviates the need to use xenografts or immune suppressed mice.

2.2. Cell Care

2.2.1. Regular Care and Passaging Procedure

The original stock of B16F1 cells was obtained from the American Type Culture Collection (ATCC) via their authorized Canadian distributor, Cedarlane Laboratories (Burlington, ON). The cells were cultured as a monolayer in 75 cm^2 flasks. The cultures were kept in a humidity controlled incubator at 37 °C and 5% CO_2 concentration while being maintained in Dulbecco's Modified Eagle's Medium supplemented with 10% fetal bovine serum (DMEM-10).

The cells were passaged prior to reaching confluence, every 2-3 days. In order to passage the cells, the old DMEM-10 was first drawn out of the flask. The cells were then rinsed with warm phosphate balanced solution (PBS) to clear away remaining growth medium. The PBS was then removed and replaced with 8 mL of trypsin-EDTA (0.25% Trypsin/0.53 mM EDTA). The flask was returned to the incubator for 6-8 minutes until the majority of cells had lifted from the flask. The trypsin-EDTA / cell solution was then drawn from the flask and added to 40 mL DMEM-10 in a conical tube. This solution was then centrifuged at 800 rpm for 8 minutes. The DMEM-10 was drawn off and the cell pellet was resuspended in 5 mL DMEM-10. The concentration of cells in this suspension was counted using a heamocytometer. The cells were then plated in 75 cm^2 flasks at a concentration of 1-2 $x10^5$ cells/mL.

2.2.2. Cell Harvesting Procedure

In order to prepare a cell suspension for inoculation, a sub-confluent flask was rinsed and trypsinized as described above. The trypsin / cell solution was then added to 40 mL of cold DMEM-10 and centrifuged at 800 rpm for 8 minutes at 4 °C. The cell pellet was then resuspended in 5 mL of cold Hank's Balanced Salt Solution (HBSS), and passed through a cell strainer with a 40 μm mesh in order to remove any cell clumps. The concentration of cells in the filtered HBSS cell suspension was then counted in a heamocytometer and adjusted to $1x10^6$ cells/mL. The cell suspension was then placed in an insulated cooler in order to be transported to the TMDT for inoculation.

2.3. Inoculation Procedure

It took approximately 15 minutes to transport the cell suspension to the TMDT after preparation. The order of inoculations was determined prior to the procedure by randomly ordering the numbers from 1-16. The mice were inoculated in corresponding order by a Registered Master Laboratory Animal Technician, and then returned to their original cages. Each mouse received a subcutaneous injection of $2x10^5$ cells (200 μL of the prepared cell suspension) to the right hind flank.

2.4. Description of GE Locus Ultra

All the imaging was performed on the GE Locus Ultra housed in the Spatial and Temporal Targeting for Amplification of Radiation Response (STTARR) lab in the TMDT. This is a fast volumetric micro-CT scanner featuring a 1024x1024 element amorphous silicon flat panel detector with 200 μm^2 pitch. The x-ray source is a clinical x-ray tube with 0.9 x 0.7 mm^2 focal spot capable of supporting voltages from 20-140 kV and currents in the range of 40 to 200 mA. The system has inherent filtration equal to 1.2 mm Al and an additional 0.15 mm Cu is used to remove low energy x-rays. The source to isocentre distance is 50.3 cm and the source to detector distance is 70.1 cm, resulting in a magnification factor of 1.3 and reconstructed images with isotropic voxel spacing of 0.15 mm.

2.5. Imaging Procedure and Protocols

2.5.1. Imaging Procedure

Prior to performing any scanning, the Isoflurane anesthesia system was set up (Figure 2.1). The anesthesia system consists of an adjustable Isoflurane pump, adjustable oxygen gas intake, an induction chamber, tubing capped with a nozzle which carries the gases from the pump to the scanner bed and tubing that can be switched between valves on the anesthesia machine to direct the flow of gases to the induction chamber or to the scanner bed as desired. The system uses a charcoal filter to scavenge the waste gases (not shown).

After the anesthesia system was in place, the scanner was put through its warm-up sequence and bright/dark fields were acquired for each of the imaging protocols.

Figure 2.1 Anesthesia machine set up for scanning.

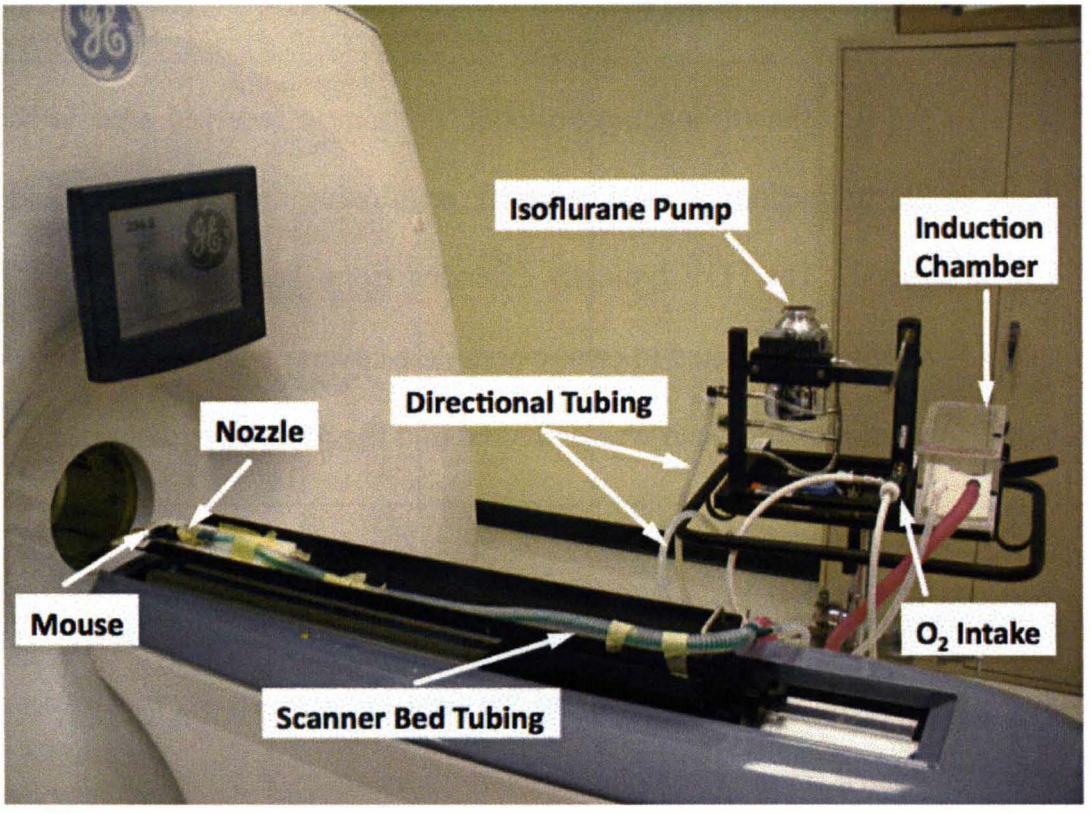

The mouse to be imaged was placed in the anesthetic induction chamber with oxygen gas flowing through at a rate of 1 L/min and an Isoflurane concentration of 3%. The mice were in the induction chamber for approximately one minute before being anesthetized and ready for scanning. Next the directional tubing of the anesthetic machine was switched such that the anesthetic gases were flowing through the tubing fixed to the bed of the scanner. The Isoflurane concentration was reduced to 1.5% and the mouse was transferred from the induction chamber to the scanner bed with its nose placed in the

nozzle at the end of the tubing. The mouse was then oriented parallel to the scanning axis, at the centre of the scanning field, with the assistance of positioning lasers. The positioning lasers appear on the retracted bed, showing the alignment of the radiation field with a crosshair at the centre of the field.

Prior to undergoing the designated imaging protocol, the mouse received a scout scan. The scout image (a 2D projection) is used to verify positioning and select the field of view (FOV) to be imaged. The FOV typically extended from the mouse's neck to the base of the tail and was always selected to ensure complete coverage of the tumour. After choosing the FOV, the appropriate scan was delivered and the mouse was returned to its cage.

The imaging procedure was repeated for each of the remaining mice in that group, then that cage was returned to the holding room and the next imaging group was retrieved. The procedure was repeated for the remaining imaging groups.

2.5.2. Imaging Protocols

After the mice had received their inoculations they were sorted into cages, and each cage was assigned to one of four specific imaging protocols: control group (which receives no imaging), low dose group, medium dose group and the high dose group. The scan parameters are displayed in Table 2.1 for each of the imaging groups.

Table 2.1 Scanning parameters for the imaging protocols used.

Imaging Group	Protocol Type	Scan Time (s)	Tube Voltage (kV)	Tube Current (mA)	Dose to air (cGy)
Low Dose	Anatomical Scan	8	80	70	7
Medium Dose	Respiratory Gated Scan	30	80	50	17
High Dose	Cardiac Gated Scan	50	80	50	28

These imaging protocols were selected to be representative of imaging that may be performed as part of a longitudinal oncology study. The low dose scan is an anatomical scan, used to simply image the internal anatomy of the subject. The medium dose scan is a protocol that could be used as part of a respiratory gated imaging session, while the high dose scan could be used as part of a cardiac gated imaging session. These imaging protocols are all typical protocols used on this scanner.

Each of the animals in the imaging groups underwent their imaging protocol a total of four times: once every four days, starting on the fourth day post inoculation. The mice were imaged at the same time of day at each of the scanning time points. After the final

imaging session, all the animals were euthanized in a CO_2 chamber and prepared for the post mortem procedure.

2.6. Post-mortem Procedure

As a result of the injection procedure this tumour model tends to grow in one large lesion at the injection site, in a region between the skin and a fat pad. The tumours were removed by first exposing the tumour with a cut in the skin next to the tumour. With the cancer exposed, it was removed by carefully cutting around the periphery using dull tip surgical scissors. Once the tumour had been excised, any excess fat or skin was trimmed away to leave only tumour tissue.

The tumour was then weighed on an electronic balance and transferred to a specimen jar. The sample was submerged in ethyl alcohol in order to fix the tissue and to provide contrast for the final tumour volume measurement. After all the tumours had been removed and jarred, the specimen jars were scanned using the low dose anatomical imaging protocol. This final scan provided an image with the contrast required to use an auto-segmentation algorithm to measure the final volume of the tumours.

After being scanned, the tissue samples were transferred to a 10% neutral buffered formalin solution. The samples were allowed to fix for 48 hours before being sent for histology.

2.7. Tumour Volume Measurements

All the tumour volume measurements were taken from the acquired images using the MicroView software package (GE Healthcare, London ON).

2.7.1. In Vivo Tumour Volume Measurements

In order to measure the volume of the tumour from the *in vivo* images, the boundary of the tumour must be contoured manually on each slice of the image that it appears in. A user performs manual contouring by placing 'nodes' with the computer mouse along the perimeter of the tumour. Adjacent nodes are then connected to one another by a curve based on a user-selected mode of interpolation. For the purpose of this study, the 'spline' interpolation provided greatest ease of use.

Once the tumour has been completely contoured, MicroView takes the set of contours and converts them into a 3D region of interest. The final tumour volume is taken as the volume contained in that region.

2.7.2. Ex Vivo Tumour Volume Measurements

The contrast offered by the ethyl alcohol allows for the use of a seeded region growing (SRG) algorithm (included in MicroView) to take volume measurements of the excised tumours. The SRG algorithm requires two inputs from the user, a CT# threshold and the selection of a seed voxel. The algorithm will then count every voxel connected to the seed voxel that has a CT# above the threshold. The algorithm then sums the volumes of the counted voxels to calculate the total volume of the region.

2.7.3. Threshold Selection

In order to select the correct threshold, images of four excised tumours representing the range of tumour volumes were selected for analysis. The excised tumour was first cropped from the image of the specimen jar to create a new image containing the entire tumour and some surrounding ethyl alcohol. The SRG algorithm was then run on the new image at many different CT# thresholds, from the same seed voxel near the centre of the tumour. The same seed voxel was found each time based on coordinates in the image provided by MicroView.

The ethyl alcohol surrounding the sample is of uniform composition, however due to image noise the CT# of the ethyl alcohol has a Gaussian distribution. By selecting the threshold at a point that corresponds to the tail of the distribution (the mean plus two standard deviations, i.e. greater than 97% of the ethyl alcohol) we are ensuring that the algorithm will not be selecting the vast majority of the ethyl alcohol, leaving it to select the voxels containing the tumour.

Figure 2.2 depicts the behavior of the SRG volume vs. CT# threshold for a range of tumour sizes.When the threshold is sufficiently low, the algorithm will select the entire image (all the tumour tissue and all the surrounding alcohol as seen at the leftmost point in Figure 2.2). As the threshold is increased above the mean CT# of ethyl alcohol the volume selected by algorithm decreases rapidly.

The *rate of decrease* in SRG volume vs. CT# threshold changes abruptly at the point where the algorithm is no longer selecting the surrounding alcohol. This point also

corresponds with the tail end of the ethyl alcohol distribution. This threshold (CT# -206) is taken as the optimal threshold, and the final tumour volume is taken as the SRG selected volume when the algorithm is run at this threshold. The same threshold was used by the region growing algorithm to take each of the excised tumour volume measurements.

Figure 2.2 The graphs depicts the abrupt change in the rate of decrease of seeded region growing algorithm selected volume vs. CT# threshold. The distribution of ethyl alcohol CT#'s are overlaid.

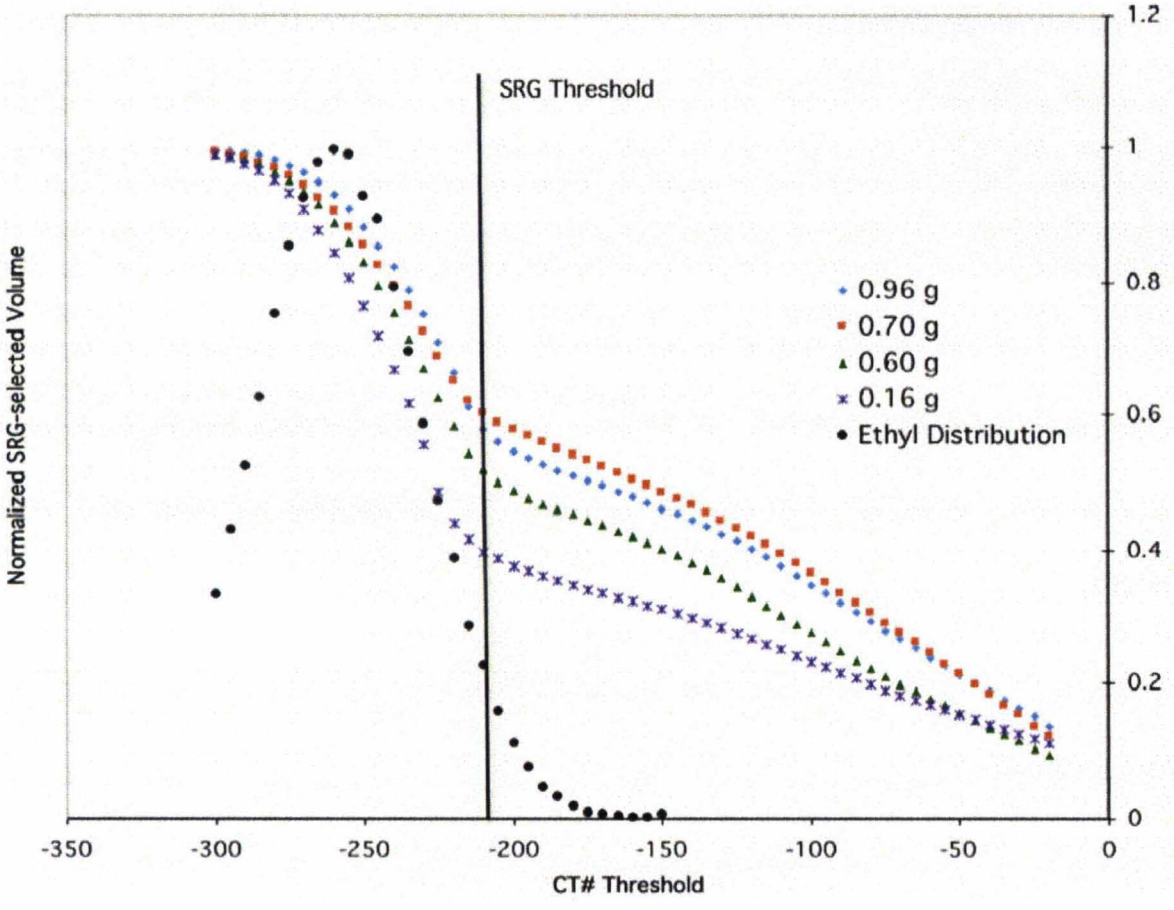

2.8. Statistical Analysis

In order to detect any effect on tumour growth from the longitudinal imaging, the mean final tumour volumes (as measured in the *ex vivo* images) of the different groups were compared using the ANOVA framework. All statistical analysis was performed using SPSS v.16.0 (SPSS Inc, Chicago IL).

2.9. Exposure Measurements

Exposure measurements were performed with an NRC calibrated (March 27, 2009) farmer type ionization chamber (NE model 2571) and electrometer (Fluke model 35040). The chamber's 0.6 cm^3 sensitive volume was oriented parallel to the scanner bed at the beam isocentre. Measurements were taken in open air with room temperature of 22.0 °C and air pressure of 758.6 mmHg. Prior to taking the exposure measurements, the scanner was put through its warm-up sequence and bright/dark fields were acquired. The total charge accumulated in the chamber was measured three times for each imaging protocol used in this study, with the average reading used for subsequent exposure and dose calculations.

The exposure, X (R), at isocentre can be calculated from the above data using the following formula:

$$X = M_C N_X \tag{2.1}$$

with,

$$M_C = M_{raw} P_{TP} P_{leak} P_{ion} P_{pol} P_{elec} P_{rp} \quad (2.2)$$

where M_c is the corrected electrometer reading, N_X is the calibration coefficient (provided by NRC in units of R/nC) at 80 kV generating potential, M_{raw} is uncorrected electrometer reading in nC, P_{TP} is the air temperature and pressure correction, P_{leak} is a correction for leakage current or detector drift in the absence of a radiation field, P_{ion} corrects for the incomplete collection of the charge generated in the chamber, P_{pol} is a factor to accommodate the fact that changing the sign of the charge being collected will change the amount of charge accumulated, P_{elec} accounts for changes in instrument sensitivity when the electrometer is operated on a scale other than the scale used for calibration and P_{rp} is a correction for radial variation of the intensity of the radiation field over the sensitive volume of the chamber. The exposure measurements were taken under conditions similar to the calibration conditions. As a result P_{ion}, P_{pol}, P_{elec} and P_{rp} are all taken as unity. P_{TP} and P_{leak} are determined by the following equations:

$$P_{TP} = \frac{760}{P} \times \frac{T + 273.15}{295.15} \quad (2.3)$$

$$P_{leak} = 1 - Bt/M_{raw} \quad (2.4)$$

where P and T are the air pressure (mmHg) and temperature (°C) at the time of measurement, B is the leakage rate and t is the acquisition time. The leakage current contributed a negligible charge to the electrometer reading and was assumed to be zero in these calculations.

After applying these correction factors and the calibration coefficients to the raw meter reading, we are left with the exposure at isocentre due to each of the imaging protocols. The dose in air can also be estimated from these measurements. The energy deposited by the x-rays in air, E_{air} is related to the charge released in air (which is the corrected meter reading, M_c) by:

$$E_{air} = (W/e)_{air} M \tag{2.5}$$

where $(W/e)_{air}$ is the energy required to produce an ion pair in air (33.9 J/C). The dose to the air (J/kg or Gy) at isocentre can then be calculated as:

$$D_{air} = \frac{E_{air}}{m_a} \tag{2.6}$$

where m_a is the mass of air within the ion chamber's sensitive volume.

Chapter 3

3. Results and Discussion

3.1. Results of Exposure Measurements

The results of the exposure measurements are displayed in Table 3.1. The average of three raw meter readings is presented ± one standard deviation. According to the calibration document for this ion chamber – electrometer pair, the calibration coefficient has an uncertainty of ± 1%. This uncertainty is included in Table 3.2, along with the exposure and dose to air at isocentre for each of the imaging protocols used.

Table 3.1 Imaging protocol parameters and associated average raw meter readings.

Imaging Protocol	Tube Potential (kV)	Tube Current (mA)	Scan Time (s)	Average Raw Meter Reading (nC)
Low Dose	80	70	8	1.526 ± 0.003
Medium Dose	80	50	30	3.979 ± 0.005
High Dose	80	50	50	6.615 ± 0.002

Table 3.2 Exposure and dose to air at isocentre for each of the imaging protocols.

Protocol	Corrected Meter Reading (nC)	Exposure (R)	Dose to Air (cGy)
Low Dose	1.528 ± 0.003	7.5 ± 0.1	6.6 ± 0.1
Medium Dose	3.986 ± 0.005	19.5 ± 0.2	17.1 ± 0.2
High Dose	6.627 ± 0.002	32.5 ± 0.3	28.5 ± 0.3

It should be noted that the exposure rate for each of these protocols is approximately 0.013 R/mA-s. This exposure rate, and the dose to air values in Table 3.2 are in agreement with the exposure rate and dose values reported elsewhere (Ford *et al.* 2007, Ford *et al.* 2006 and Graham *et al.* 2008) for the same model scanner and imaging protocols.

3.2. Comparison of *In Vivo* and *Ex Vivo* Tumour Volume Measurements

The *in vivo* final tumour volume measurements were frequently made difficult by the poor contrast between the tumour and the surrounding tissue (Figure 3.1). Even with optimal window and level settings it can be very difficult to delineate the boundary of the growth. As a result, the contours may not accurately represent the boundary of the tumour. This adds an uncertainty to any volume measurements taken from these *in vivo*

images. Despite the difficulties contouring, Figure 3.2 shows a decent correlation (R^2=0.9535) between tumour mass and volume measured *in vivo*, indicating that the technique can provide reasonably reliable results.

Figure 3.1 An *in vivo* image of a tumour-bearing mouse. The arrow indicates the location of the tumour.

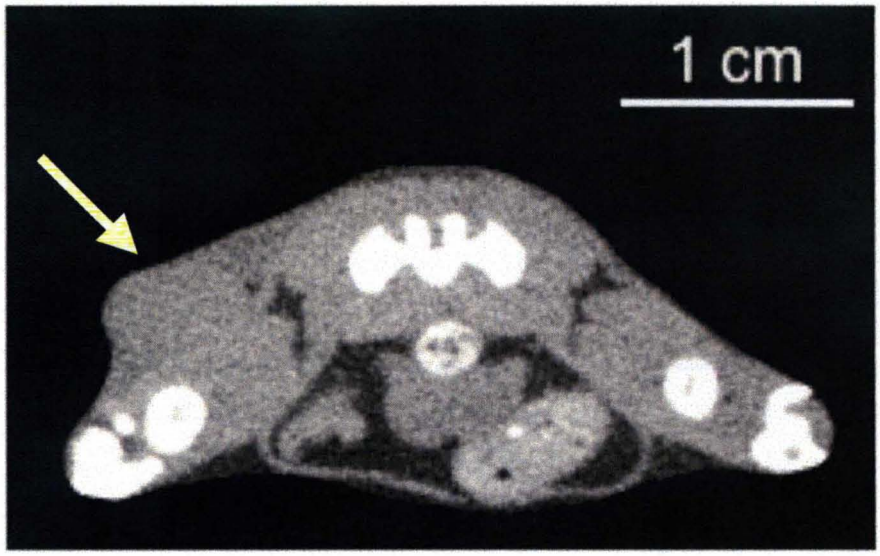

The *ex vivo* tumour volume measurements were performed using the SRG algorithm included in Microview. Figure 3.3 is a representative image of the excised tumours in ethyl alcohol. After selecting the threshold, as described in section 2.8, all tumour volume measurements were performed at that threshold. A linear regression (shown in Figure 3.4) between the *ex vivo* final tumour volume and final tumour mass shows a strong correlation (R^2=0.9924), suggesting that this measurement technique is more reliable.

Figure 3.2 Final tumour volume measured *in vivo* by manual contouring vs. final tumour mass.

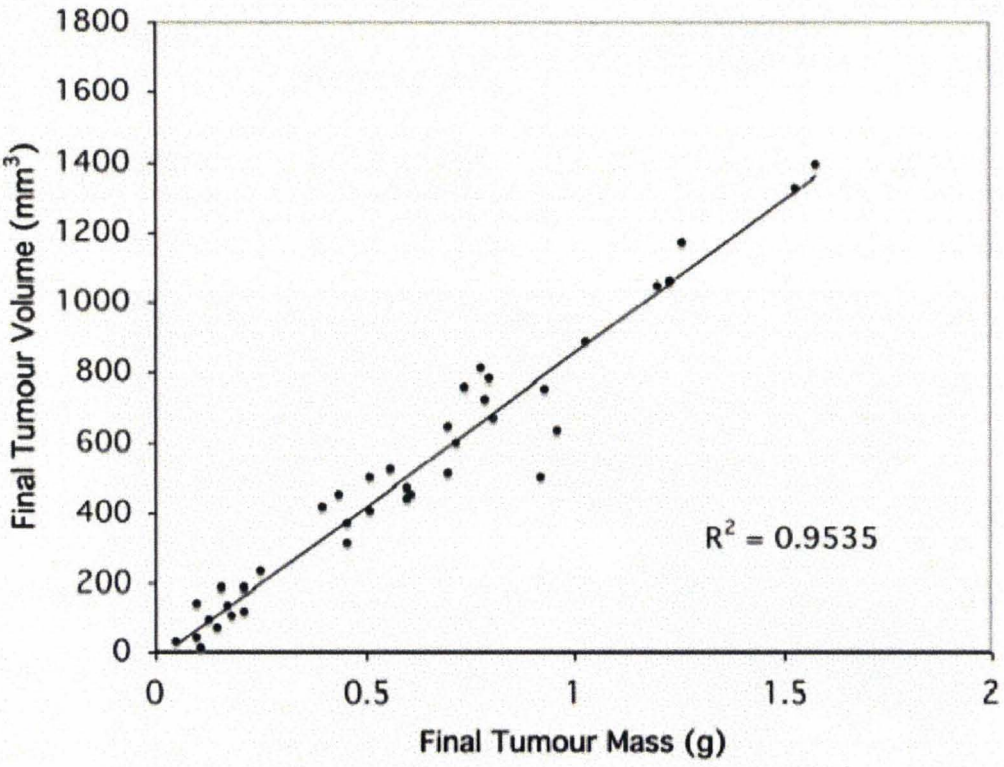

Figure 3.3 An axial slice taken from an image of the excised tumours submerged ethyl alcohol. Note the contrast between the tumours and the surrounding alcohol.

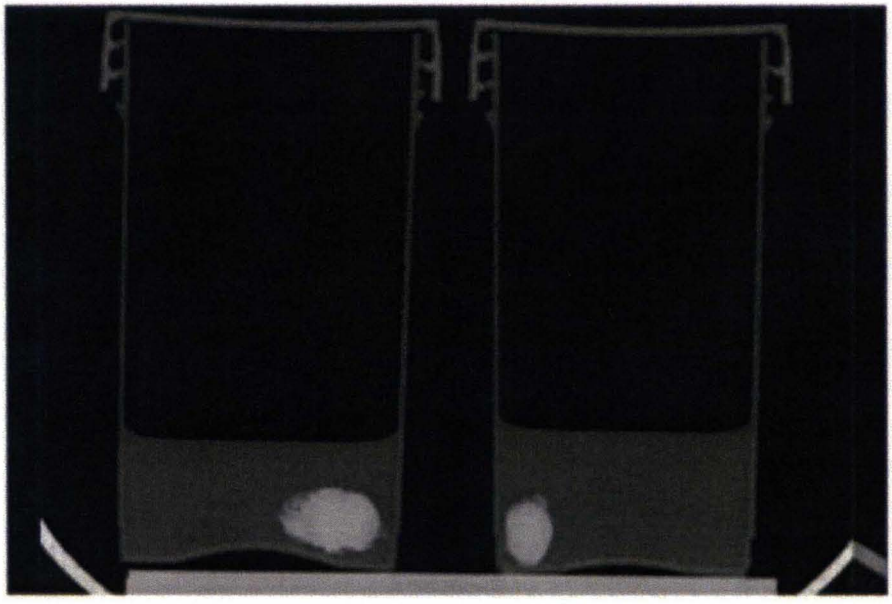

The *ex vivo* measurement technique provides more consistent results for two reasons. First, the ample contrast available between the tumour and the background drastically improves the ability of the user (or an algorithm) to confidently detect the boundary of the tumor. Secondly, the SRG algorithm uses consistent criteria (the user-selected threshold) to judge the boundary of the tumour in each data set. This removes some of the human error involved in contouring the boundary of a structure *in vivo* (Graham *et al.* 2008).

Figure 3.4 Final tumour volume measured *ex vivo* using the seeded region growing algorithm vs. final tumour mass.

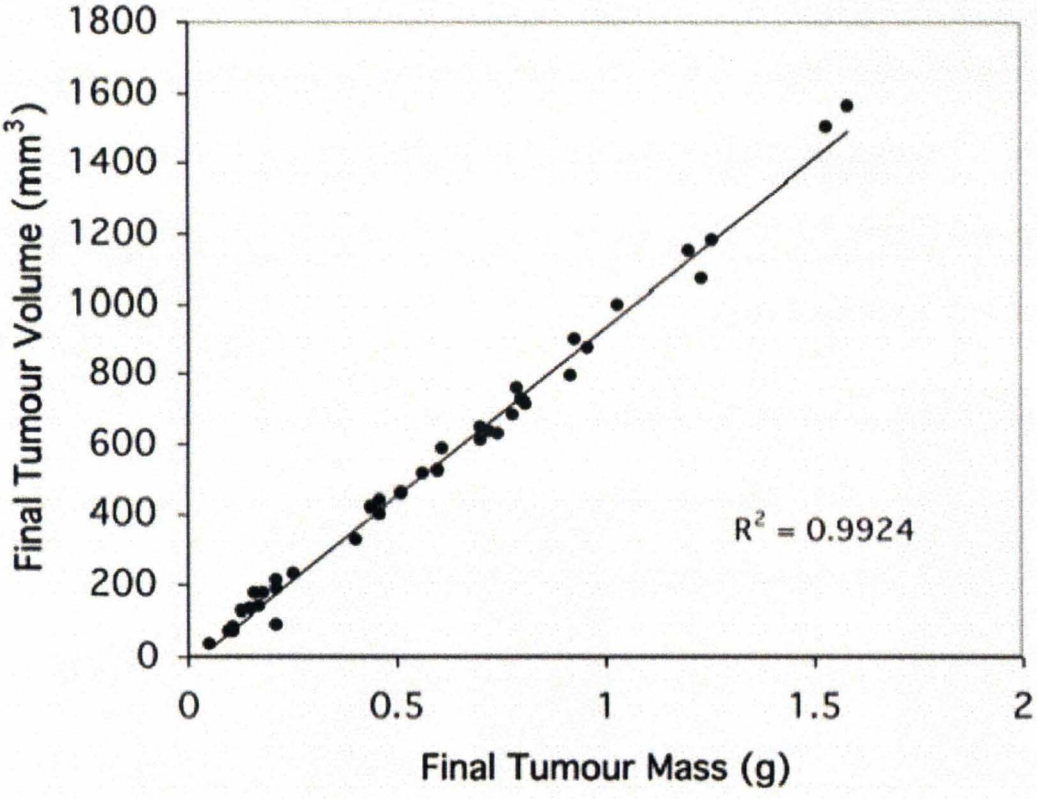

Based on the comparison of the results from the two measurement techniques, and experience taking both types of measurements, it is clear that the *ex vivo* measurement technique provides more reliable results. Therefore, the results of tumour volume measurements presented below are those gathered using the *ex vivo* measurement technique.

3.3. Results of Final Tumor Volume Measurements

The entire experimental protocol was completed on four batches of mice, with each batch consisting of four mice in each of the four imaging groups, resulting in a total of 64 mice. Eight mice did not grow tumours, or grew tumours that were not detected in the images and were too small to resect (1, 2, 1 and 4 mice from the control, low, medium and high dose groups respectively). These mice were not included in the subsequent statistical analysis. Table 3.3 shows descriptive statistics of the final tumour volumes (mm^3) by imaging group and Figure 3.5 displays the average final tumour volume by group with error bars equal to ± 1 standard error.

While the standard deviations are large relative to the means of each group, this level of variance is typical of other tumour growth studies, implying that the inoculation procedure was appropriate and tumour growth proceeded as usual.

Nguyen *et al.* (2007) used B16F10 cells in a subcutaneous tumour model in C57BL/6J as part of a gene therapy study. The control group received an initial inoculation of $1x10^5$

Table 3.3 Descriptive statistics of the final tumour volumes in mm^3 (from *ex vivo* measurements).

Group	N	Mean	Standard Deviation	Standard Error	Minimum	Maximum
Control	15	403.80	372.75	96.24	51.33	1340
Low	14	601.50	359.46	96.07	34.03	1180
Medium	15	573.16	479.95	123.92	75.52	1560
High	12	411.16	310.36	89.59	73.66	1000
Total	56	500.17	390.05	52.12	34.03	1560

Figure 3.5 A bar graph of the average final tumour volume by group. Error bars represent ± 1 standard error.

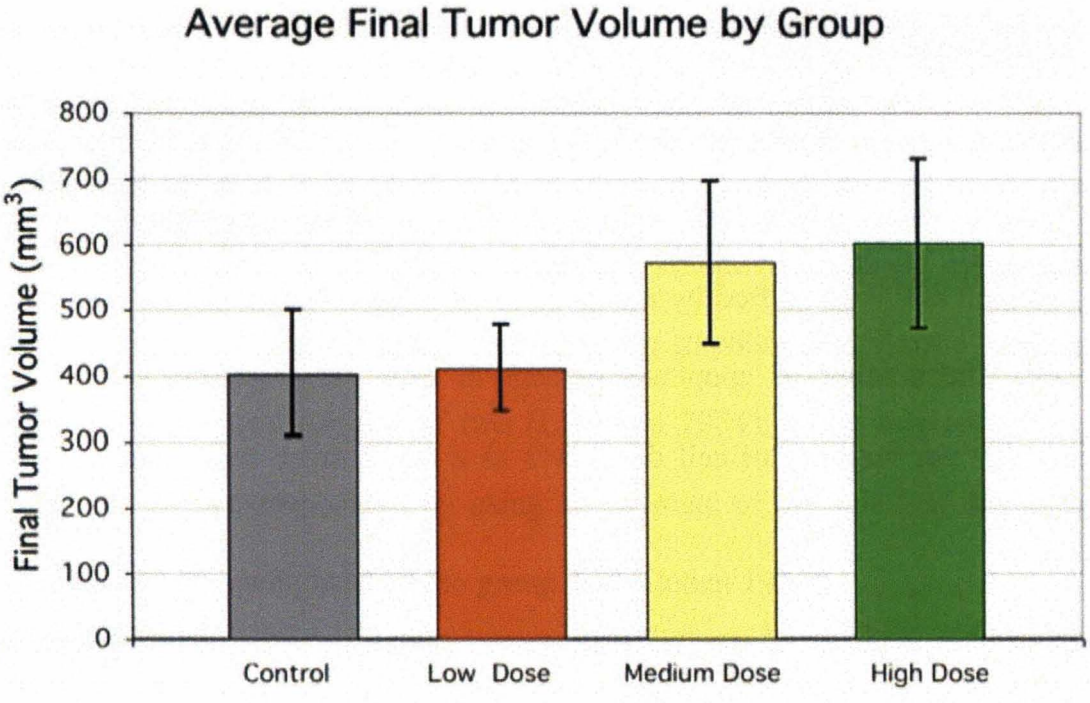

cells and five subsequent null adenovirus inoculations. By day 16 the average volume was approximately 750 mm^3 with a standard deviation of approximately 550 mm^3.

Garcia-Barros *et al.* (2003) used B16F1 cells in a subcutaneous tumour model in C57BL/6 to investigate the role of endothelial cell apoptosis in regulating tumour response to radiotherapy. As part of their investigation they implanted 10^6 cells and by day 25 the tumours averaged approximately 380 mm^3 with a standard deviation of roughly 280 mm^3.

Finally, Koga *et al.* (2008) used B16F1 cells in C57BL/6 mice as part of a gene therapy study. The control group in this study received an initial inoculation of $1x10^6$ cells and an injection of PBS at day 7. By day 13 the tumours averaged approximately 1100 mm^3 with a standard deviation of approximately 500 mm^3.

3.4. Histology

Since radiation damage causes cell death via apoptosis (Steel 2002), a TUNEL stain was used in order to detect which cells were apoptotic and which were necrotic. A positive TUNEL stained cell is identified by a concentrated reddish-brown colour at the nucleus of the cell. The amount of apoptosis present in each slide appears to be minimal, suggesting that the majority of cell death was as a result of necrosis, and not radiation damage.

Quantitative interpretation of the TUNEL stained histology was made difficult by the pigments naturally present in the melanoma. Figure 3.6 shows slides representative of

each of the imaging groups. There are no gross differences discernable between the histological results of the different groups.

Figure 3.6 Representative TUNEL stained histology from each of the groups. A) Control group B) Low dose C) Medium dose D) High dose

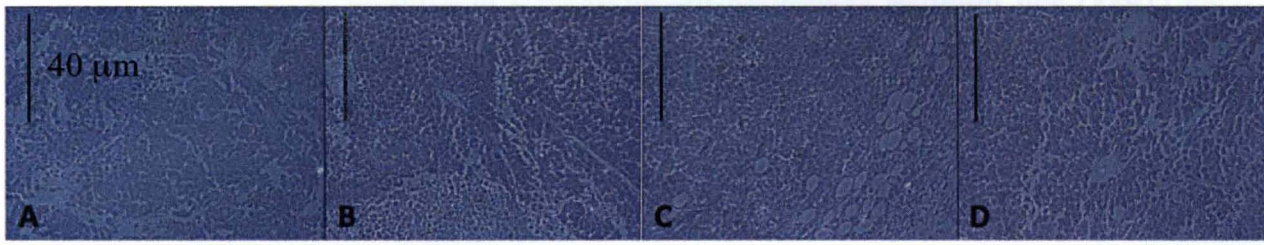

3.5. Statistical Analysis

In order to look for a difference among the mean final tumour volumes of the different groups, an analysis of variance (ANOVA) was employed. When using the ANOVA framework, one must be aware of the assumptions that are being made. Strictly speaking, ANOVA requires equal group sizes and equal variance among groups. While these assumptions are not met in the case of the final tumour volume data presented above, the ANOVA test is known to be robust to modest violations of these assumptions. In particular ANOVA will remain robust as long as the standard deviations of each group do not differ by more than a factor of two (Lindman 1974), while modest differences in group size can be accommodated by using an estimate of the standard deviation of the group means which is weighted by the group size (Cohen 1988).

The results of the ANOVA test performed in SPSS indicate no statistical difference between the average final tumour volumes in these groups (p=0.399). In order to confidently accept the null hypothesis of equal means among the groups, one must consider the power of the test. Power analysis for the ANOVA test was described by Cohen (1988) and involves specifying the alternative hypothesis in terms of a quantity referred to as the effect size.

The effect size, f, is defined as the ratio of the standard deviation of the group means, σ_m, to the pooled standard deviation of the population, σ. All three quantities are defined below (data presented in table 3.4), where n_i is the size of group i, m_i is the mean of group i, σ_i is the standard deviation of group i, m is the overall mean and N is the total sample size.

$$f = \frac{\sigma_m}{\sigma} \tag{3.1}$$

$$\sigma_m = \sqrt{\frac{\sum_{i=1}^{4} n_i (m_i - m)^2}{N}} \tag{3.2}$$

$$\sigma = \sqrt{\frac{\sum_{i=1}^{4} (n_i - 1)\sigma_i^2}{N}} \tag{3.3}$$

Based on the data collected we can confidently accept the null hypothesis (with $\alpha = 0.1$ and $\beta = 0.1$) for an effect size of $f = 0.47$.

Table 3.4 Statistical quantities used to interpret the results. Values calculated from the data presented in Table 3.3.

Quantity	Value
σ	390.1 mm^3
σ_m	183.3 mm^3
N	56
f	0.47
D	1.26

The most intuitive way to interpret the effect size in the context of the final tumour volumes is by relating the effect size to a quantity denoted 'D' – the *standardized range of population means*,

$$D = \frac{m_{max} - m_{min}}{\sigma} \tag{3.4}$$

where m_{max} is the largest of the group means, m_{min} is the smallest of the group means and σ is the pooled standard deviation as defined in equation 3.3. The standardized range of population means is a dimensionless quantity representing the range of group means relative to the pooled standard deviation.

If one were to compare only two means this way, than f and D would be related by:

$$f = \frac{1}{2}D \tag{3.5}$$

In other words, the standard deviation of any two values is equal to half their difference. If one were to compare more than two means this way, than the relationship between the standard deviation of these means (f) and the range over which these means are spread (D) will depend on the *distribution* of the means over that range. In the case of four evenly spaced means, Cohen suggests the relation:

(3.6)

With this relation in mind, an effect size of $f = 0.47$ implies a standardized range of group means spanning 491 mm^3, or approximately 1.26 times the pooled standard deviation. In other words, we can confidently reject the notion that the longitudinal imaging protocols that the animals received will cause the average final tumour volumes among the groups to span more than 1.26 times the population standard deviation. Further context for the interpretation of this effect is offered below.

3.6. Discussion

While the size of the effect that we can confidently reject is rather large, it seems likely that the effect of the longitudinal imaging on the tumour growth is small or even negligible. The total radiation doses associated with the scans is small (total doses of 0.28, 0.68 and 1.12 Gy respectively) when compared to the radiation doses typically administered as part of a radiotherapy treatment. For example, Medina *et al.* (2008)

irradiated subcutaneous tumours grown from HeLa cells in mice to a total of 50 Gy at 2.5 Gy/day over twenty days and saw a significant difference in tumour volume when compared to control. That treatment schedule caused an effect of size f = 0.78 corresponding to a standardized range of group means D = 1.56. With this in mind, it can be said that any effect on tumour growth caused by the longitudinal imaging protocol is smaller than the effect of a treatment.

Bristow *et al.* (1990) performed an *in vitro* study of the radiosensitivity of eight murine tumour cell lines, including B16F1. This study revealed that B16F1 cells are more radiosensitive than most tumour cells, and that the majority of cell death occurs at doses greater than 1 Gy. Considering that the scanner provides doses much lower than 1 Gy, it is reasonable to expect that the majority of the irradiated cells would survive the scan.

Bristow *et al.* also provided parameters that can be used to estimate the surviving fraction of B16F1 cells, *in vitro*, after receiving a specific dose. Estimates of the surviving fraction of cells having received the doses associated with each of the imaging protocols used in this study provided in Table 3.5. The surviving fraction of cells *in vitro* gives an estimate of the amount of cell death caused by the delivered dose. In a related work, Bristow showed that *in vitro* radiosensitivity correlates well with *in vivo* radioresponse (Bristow and Hill 1990).

Table 3.5 Estimates of the surviving fraction of B16F1 cells (*in vitro*) after receiving a dose representative of a micro-CT scan. The estimates are based on parameters provided by Bristow *et al.* (1990).

Irradiation level	Absorbed Dose (Gy)	Calculated Surviving Fraction (%)
Low	0.07	98.4
Medium	0.17	96.2
High	0.28	93.8
Example Treatment Dose (Medina et al. 2008)	2.5	50.8

The large surviving fraction of *in vitro* tumour cells after receiving a dose typical of a micro-CT scan indicates that these scans will do little to curb the growth of the tumour cells. For simplicity, the absorbed doses used to calculate the surviving fraction of cells were set as the entrance doses from the protocols used in this study. In reality the dose absorbed by the tumour tissue *in vivo* will be less than the entrance dose of the scan (Obenaus and Smith 2004) because other structures in the animal (such as skin, bones, muscles, fat) will absorb some of the delivered energy. Therefore the surviving cell fractions in Table 3.5 represent a worst case scenario. Also, by selecting a radiosensitive tumour cell line and performing subcutaneous inoculations (such that the tumour would not be shielded by other structures in the animal), the likelihood of causing an effect on tumour growth was thought to be maximized.

The high surviving fraction of cells indicates that the doses delivered by these scans are simply not high enough to cause considerable cell death, and therefore not high enough to significantly alter tumour growth.

Another factor likely mitigating the effect of the scanner dose was the time between scans. By allowing four days between scans, the tumour cells had plenty of time to repopulate between irradiations. B16F1 cells have a doubling time of approximately 24 hours (Netland and Zetter 1985). By allowing for 96 hours between scans, the tumour cells would have ample time to perform several doublings, thereby easily compensating for any cell death caused by the irradiation.

Considering the relatively low imaging dose and the time between scans, it is likely that effect of the imaging dose on tumour growth is negligible. We can confidently reject the notion that any effect caused is comparable in size to a radiotherapy treatment.

Chapter 4

4. Summary and Future Work

4.1 Summary

Micro-CT has proven itself as a useful tool for preclinical *in vivo* imaging, and its applications continue to expand. The physical principals of x-ray CT require that the dose delivered to the subject increases as the resolution of the image improves, and these doses start to quickly escalate in the resolution regime of micro-CT. With this in mind, many researchers have cautioned the use of micro-CT for longitudinal *in vivo* imaging studies.

This project was designed to investigate the effect that the dose delivered during a longitudinal imaging study may have on a preclinical oncology model. The mice, tumour cell line and imaging protocols were selected to be representative of oncology models and imaging studies that are being reported in the literature today. The average final tumour volume among different imaging groups was the parameter used to investigate the effect of the delivered radiation.

Four groups of mice (one control group and 3 imaging groups) underwent longitudinal micro-CT imaging. The mice in the imaging groups received a total of four scans each spaced four days apart, while the control animals received no radiation. The tumours were excised shortly following the final scan.

Final tumour volumes were measured *ex vivo* by analyzing micro-CT images of the excised tumours. This unique method provided consistent and reproducible measures of the final tumour volumes.

The results of this investigation indicate that any effect caused by the imaging is certainly smaller than the effect of a radiotherapy treatment. Based on the results of the histology and previous *in vitro* studies of this cell line, it seems likely that the effect of longitudinal micro-CT imaging on tumour growth in this study was negligible.

4.2 Future Work

Creating another group of mice to be imaged at yet higher entrance dose could be included to expand the work presented here. This group could reveal the imaging dose that causes a statistically significant difference in the final tumour volumes of this longitudinal study.

It may also be pertinent to perform a similar imaging study with more frequent scans. By escalating the dose to the tumours and reducing repopulation time between scans, a statistically significant difference in final tumour volumes may become appearent.

The variance seen in the growth of the tumours in different mice (despite the same initiating event) makes it difficult to detect small differences in average final tumour volumes without using an impractically large sample size. It may be possible to reduce this variance by altering the inoculation procedure. If the cells were suspended in a gel,

as opposed to a liquid, the inoculation would be confined to a smaller area within the animal, resulting in a more consistent inoculation and hopefully more consistent tumour growth.

The results of this work have promising implications for micro-CT imaging of small animal oncology models. The fact that there is no major affect on the growth of the tumours as a result of the longitudinal imaging will give researchers confidence that they can use micro-CT to acquire useful 3D data sets, without interfering in the growth of the tumours in their models. These data sets can be used to quantitatively and accurately assess *in vivo* tumour volumes and growth, giving researchers an imaging tool which can be used to monitor the effects of novel cancer treatments.

Bibliography

Badea, C T, Bucholz, E, Hedlund, L W, Rockman, H A and Johnson, G A 2006 Imaging methods for morphological and functional phenotyping of the rodent heart *Toxicol. Pathol.* **34** (1) 111-7

Bedea, C, Hedlund, L W, Johnson, G A 2004 Micro-CT with respiratory and cardiac gating *Med. Phys.* **31** (12) 3324-9

Bakan, D A, Longino, M A, Weichert, J P and Counsell, R E 1996 Physicochemical characterization of a synthetic lipid emulsion for hepatocyte - selective delivery of lipophilic compounds: Application to polyiodinated triglycerides as contrast agents for computed tomography *J. Pharm. Sci.* **85** (9) 908-14

Bartling, S H, Stiller, W, Semmler, W and Kiessling, F 2007 Small animal computed tomography Imaging *Current Medical Imaging Reviews* **3** (1) 45-59

Boone, J M, Velazquez, O and Cherry, S R 2004 Small-Animal X-ray Dose from Micro-CT *Molecular Imaging* **3** (3) 149-58

Bristow, R G, Hardy, P A and Hill, R P 1990 Comparison between In Vitro radiosensitivity and In Vivo radioresponse of murine tumor cell lines. I. Parameters of In Vitro radiosensitivity and endogenous cellular glutathione levels *Int. J. Radiat. Oncol. Biol. Phys.* **18** (1) 133-45

Bristow, R G and Hill, R P 1990 Comparison between In Vitro radiosensitivity and In Vivo radioresponse in murine tumor cell lines H. In Vivo radioresponse following fractionated treatment and In Vitro/In Vivo correlations *Int. J. Radiat. Oncol. Biol. Phys.* **18** (2) 331-45

Carlson, S K, Classic, K L, Bender, C E and Russell, S J 2007 Small animal absorbed radiation dose from serial micro-computed tomography imaging *Molecular Imaging and Biology* **9** (2) 78-82

Cavanaugh, D, Johnson, E, Price, R E, Kurie, J, Travis, E L and Cody, D D 2004 In Vivo Respiratory-Gated Micro-CT Imaging in Small-Animal Oncology Models *Molecular Imaging* **3** (1) 55-62

Chun, I K, Cho, M H, Park, J and Lee, S Y 2006 In vivo trabecular thickness measurement in cancellous bones: longitudinal rat imaging studies *Physiol. Meas.* 8 695-702

Cohen, J 1988 *Statistical Power Analysis for the Behavioral Sciences* (Hillsdale, N.J.: L. Erlbaum Associates)

Drangova, M, Ford, N L, Detombe, S A, Wheatly, A R, Holdsworth, D W 2007 Fast Retrospectively Gated Quantitative Four-Dimensional(4D) Cardiac Micro Computed Tomography Imaging ofFree-Breathing Mice *Invest. Radiol.* **42** (2) 85-94

Faulkner, K and Moores, B M 1984 Noise and contrast detection in computed tomography images *Phys. Med. Biol.* 4 329-339

Feldkamp, L A, Davis, L C and Kress, J W 1984 Practical cone-beam algorithm *J. Opt. Soc. Am. A* **1** (6) 612-9

Figueroa, S D, Winkelmann, C T, Miller, W H, Volkert, W A and Hoffman, T J 2008 TLD assessment of mouse dosimetry during microCT imaging *Med. Phys.* **35** (9) 3866-74

Ford, N L, Thornton, M M and Holdsworth, D W 2003 Fundamental image quality limits for microcomputed tomography in small animals *Med. Phys.* **30** (11) 2869-77

Ford, N L, Wheatley, A R, Holdsworth, D W and Drangova, M 2007 Optimization of a retrospective technique for respiratory-gated high speed micro-CT of free-breathing rodents *Phys. Med. Biol.* 19 5749-69

Ford, N L, Graham, K C, Groom, A C, MacDonald, I C, Chambers, A F and Holdsworth, D W 2006 Time-Course Characterization of the Computed Tomography Contrast Enhancement of an Iodinated Blood-Pool Contrast Agent in Mice Using a Volumetric Flat-Panel Equipped Computed Tomography Scanner *Invest. Radiol.* **41** (4) 384-90

Ford, N, Nikolov, H, Norley, C D, Thornton, M, Foster, P, Drangova, M and Holdsworth, D 2005 Prospective respiratory-gated micro-CT of free breathing rodents *Med. Phys.* **32** (9) 2888-98

Garcia-Barros, M, Paris, F, Cordon-Cardo, C, Lyden, D, Rafii, S, Haimovitz-Friedman, A, Fuks, Z and Kolesnick, R 2003 Tumor response to radiotherapy regulated by endothelial cell apoptosis *Science* **300** (5622) 1155-9

Graham, K C, Wirtzfeld, L A, MacKenzie, L T, Postenka, C O, Groom, A C, MacDonald, I C, Fenster, A, Lacefield, J C and Chambers, A F 2005 Three-dimensional high-frequency ultrasound imaging for longitudinal evaluation of liver metastases in preclinical models *Cancer Res.* **65** (12) 5231-7

Graham, K C, Ford, N L, MacKenzie, L T, Postenka, C O, Groom, A C, MacDonald, I C, Holdsworth, D W, Drangova, M and Chambers, A F 2008 Noninvasive Quantification of Tumor Volume in Preclinical Liver Metastasis Models Using Contrast-Enhanced X-Ray Computed Tomography *Invest. Radiol.* **43** (2) 92-9

Johns, P C and Yaffe, M 1982 Scattered radiation in fan beam imaging systems *Med. Phys.* **9** (2) 231-9

Knoll, G 2000 *Radiation Detection and Measurement* (New York: John Wiley & Sons)

Koga, M *et al.* 2008 Mutant MCP-1 therapy inhibits tumor angiogenesis and growth of malignant melanoma in mice *Biochem. Biophys. Res. Commun.* **365** (2) 279-84

Lindman, H R 1974 *Analysis of Variance in Complex Experimental Designs.* (San Francisco: W.H. Freeman)

Liu, Z, Yang, G, Lee, Y Z, Bordelon, D, Lu, J and Zhou, O 2006 Carbon nanotube based microfocus field emission x-ray source for microcomputed tomography *Appl. Phys. Lett.* **89** (10) 103-11

Medina, L, Herrera-Penilla, B, Castro-Morales, M, Garcia-Lopez, P, Jurado, R, Perez-Cardenas, E, Chanona-Vilchis, J and Brandan, M 2008 Use of an orthovoltage X-ray treatment unit as a radiation research system in a small-animal cancer model *Journal of Experimental & Clinical Cancer Research* **27**:57

Motz, J W and Danos, M 1978 Image information content and patient exposure *Med. Phys.* **5** (1) 8-22

Netland, P and Zetter, B 1985 Metastatic potential of B16 melanoma cells after in vitro selection for organ-specific adherence *J. Cell Biol.* **101** (3) 720-4

Nguyen, N, Cornet, A, Blacher, S, Tabruyn, S P, Foidart, J, Noel, A, Martial, J A and Struman, I 2007 Inhibition of Tumor Growth and Metastasis Establishment by Adenovirus-mediated Gene Transfer Delivery of the Antiangiogenic Factor 16K hPRL *Mol. Ther.* **15** (12) 2094-100

Nyman, J S, Munoz, S, Jadhav, S, Mansour, A, Yoshii, T, Mundy, G R and Gutierrez, G E 2009 Quantitative measures of femoral fracture repair in rats derived by micro-computed tomography *J. Biomech.* **42** (7) 891-7

Obenaus, A and Smith, A 2004 Radiation dose in rodent tissues during micro-CT imaging *Journal of X-Ray Science & Technology* **12** (4) 241-9

Paulus, M, Gleason, S, Easterly, M and Foltz, C 2001 A review of high resolution X-ray computed tomography and other imaging modalities for small animal research *Lab Animal* **30** (3) 36-45

Podgorsak, E B 2006 *Radiation Physics for Medical Physicists* (New York: Springer)

Prince, J L 2006 *Medical Imaging Signals and Systems* ed J M Links (Upper Saddle River, N.J.: Pearson Prentice Hall)

Ross, W, Cody, D, Hazel, J 2006 Design and performance characteristics of a flat-panel computed tomography system *Medical Physics* **33** (6) 1888-1901

Safwat, A, Aggerholm, N, Roitt, I, Overgaard, J and Hokland, M 2004 Tumour burden and interleukin-2 dose affect the interaction between low-dose total body irradiation and interleukin 2 *Eur. J. Cancer* **40** (9) 1412-7

Siewerdsen, J H and Jaffray, D A 2001 Cone-beam computed tomography with a flat-panel imager: Magnitude and effects of x-ray scatter *Med. Phys.* **28** (2) 220-31

Sonke, J, Zijp, L, Remeijer, P and van Herk, M 2005 Respiratory correlated cone beam CT *Med. Phys.* **32** (4) 1176-86

Steel, G 2002 *Basic clinical radiobiology*, 3rd ed. (New York: Oxford University Press, London.)

Taschereau, R, Chow, P L and Chatziioannou, A F 2006 Monte Carlo simulations of dose from microCT imaging procedures in a realistic mouse phantom *Med. Phys.* **33** (1) 216-24

Walters, E B, Panda, K, Bankson, J A, Brown, E and Cody, D D 2004 Improved method of in vivo respiratory-gated micro-CT imaging *Phys. Med. Biol.* **49** (17) 4163-72

Wang, D G and Vannier, D M 2001 Micro-CT Scanners for Biomedical Applications: An Overview *Advanced Imaging* **16** (7) 18-27

Weber, S M, Peterson, K A, Durkee, B, Chen, Q, Longino, M, Warner, T, Lee, F T and Weichert, J P 2004 Imaging of murine liver tumor using MicroCT with a hepatocyte-selective contrast agent: Accuracy is dependent on adequate contrast enhancement *J. Surg. Res.* **119** (1) 41-5

Weichert, J P, Lee, F T, Chosy, S G, Longino, M A, Kuhlman, J E, Heisey, D M and Leverson, G E 2000 Combined hepatocyte-selective and blood-pool contrast agents for the CT detection of experimental liver tumors in rabbits *Radiology* **216** (3) 865-71